

# Atmospheric data support a multi-decadal shift in the global methane budget towards natural tropical emissions

Alice Drinkwater<sup>1,2</sup>, Paul I. Palmer<sup>1,3</sup>, Liang Feng<sup>1,3</sup>, Tim Arnold<sup>2,1</sup>, Xin Lan<sup>4,5</sup>, Sylvia E. Michel<sup>6</sup>, Robert Parker<sup>7,8</sup>, and Hartmut Boesch<sup>7,8</sup>

<sup>1</sup>School of GeoSciences, University of Edinburgh, Edinburgh, UK

<sup>2</sup>National Physical Laboratory, Teddington, UK

<sup>3</sup>National Centre for Earth Observation, University of Edinburgh, Edinburgh, UK

<sup>4</sup>Cooperative Institute for Research in Environmental Sciences, University of Colorado Boulder, Boulder, CO, USA

<sup>5</sup>Global Monitoring Laboratory, National Oceanic and Atmospheric Administration, Boulder, CO, USA

<sup>6</sup>Institute of Arctic and Alpine Research, University of Colorado Boulder, Boulder, CO, USA

<sup>7</sup>National Centre for Earth Observation, Space Park Leicester, University of Leicester, UK

<sup>8</sup>Earth Observation Science, School of Physics and Astronomy, University of Leicester

**Correspondence:** Paul I. Palmer (paul.palmer@ed.ac.uk)

**Abstract.** We use the GEOS-Chem global 3-D model and two inverse methods (the Maximum *A Posteriori* and Ensemble Kalman Filter) to infer regional methane (CH<sub>4</sub>) emissions and the corresponding ~~carbon-stable~~ stable carbon isotope source signatures, 2004–2020, across the globe using *in situ* and satellite remote sensing data. Over our 17-year study period, we find ~~consistent evidence from both atmospheric CH<sub>4</sub> datasets of using the *in situ* data~~ a progressive increase of CH<sub>4</sub> emissions ~~at tropical (30N to 30S) latitudes (+3.80 from tropical continental regions (3.6 Tg/yr/yr), including North Africa, tropical South America, and Tropical Asia. The second largest increase in CH<sub>4</sub> emissions over this period (1.6 Tg/yr/yr) is from China. For Boreal regions we estimate a net decrease of -0.2 Tg/yr/yr and for northern and southern temperate regions we estimate trends of 0.03 Tg/yr/yr and 0.2 Tg/yr/yr, respectively. The increase in tropical CH<sub>4</sub> emissions is~~ accompanied by a progressively isotopically lighter atmospheric  $\delta^{13}\text{C}$  signature ~~, consistent with increasing biogenic wetland emissions. The highly-resolved satellite from the tropics, particularly since 2012, which is consistent with an increased biogenic emission source. Over China, we find a weaker trend towards isotopically lighter  $\delta^{13}\text{C}$  sources, suggesting that heavier isotopic source signatures play a larger contribution to this region. Satellite remote sensing data provide evidence of additional evidence of emission hotspots of CH<sub>4</sub> that are consistent with the location and seasonal timing of wetland emissions, limiting the hypothesis about the hydroxyl radical (OH) sink for CH<sub>4</sub> playing a significant role in observed global growth in atmospheric.~~ The collective evidence suggests that increases in tropical CH<sub>4</sub> ~~We find that since 2004, the largest growing regional contributions (2004–2020) are from North Africa (+19.9 Tg/yr), China (+21.6 Tg/yr), and Tropical South America (+14.2 Tg/yr). To quantify emissions are from biogenic sources, with a significant fraction from wetlands. To understand~~ the influence of our results to changes in ~~OH~~ the oxidation of atmospheric CH<sub>4</sub> by the hydroxyl radical (OH), we also report regional CH<sub>4</sub> emission estimates using an alternative scenario of a 0.5%/yr decrease in OH since 2004, followed by a 5 larger 1.5% drop in 2020 during the first COVID-19 lockdown. We find that our main findings are robust against those idealised year-to-year changes in OH~~,~~ although they are inconsistent with global-scale constraints on estimates of the global mean atmospheric growth of atmospheric CH<sub>4</sub>.

## 1 Introduction

Changes in atmospheric methane ( $\text{CH}_4$ ) over the last few decades have unfolded without clear explanation, exposing inadequacies in our measurement coverage and our ability to definitively attribute those changes to individual emissions and losses. The climatic importance of atmospheric  $\text{CH}_4$  lies in its ability to absorb and emit infrared radiation at wavelengths that are relevant to outgoing terrestrial radiation and incoming shortwave radiation (Allen et al., 2023). Consequently, atmospheric  $\text{CH}_4$  helps to maintain Earth's radiative balance and surface and atmospheric temperatures. Atmospheric  $\text{CH}_4$  is derived from emissions due to thermogenic (organic matter broken down at high temperatures and pressures, mainly released during extraction and transport of fossil fuels), pyrogenic (through incomplete combustion of organic matter), and biogenic (microbial activity) based production pathways. The main loss process is from the hydroxyl radical (OH), with minor losses from the reaction with chlorine, uptake from soils, and stratospheric loss.  ~~$\text{CH}_4$  Methane is the second most abundant anthropogenic greenhouse gas and has a  $\text{GWP}_{100}$  value of 28 (Masson-Delmotte et al., 2021), a widely used metric that estimates, for a given mass emission, the influence on capturing heat in the atmosphere over 100 years. A mass emission of  $\text{CH}_4$  is therefore 28 times more powerful at capturing heat in the atmosphere than an equivalent mass emission of carbon dioxide~~ in terms of its anthropogenic radiative forcing. The global  $\text{CH}_4$  growth rate was close to zero from 2000 to 2006 (Dlugokencky et al., 2020) but has since accelerated, with ~~global yearly~~ a global annual growth rate reported by NOAA exceeding 15 ppb for the first time in 2020 ~~(?)~~ and more than 18 ppb in 2021 (Feng et al., 2023). Concurrently, we are witnessing a progressively isotopically lighter signature of global averaged  $\text{CH}_4$  (more negative global average atmospheric  $\delta^{13}\text{C}$  value), ~~possibly indicative of changing contributions of emissions sources, for example an increase in biogenic sources or a decrease in thermogenic sources (Lan et al., 2021)~~. Analysis of  $\text{CH}_4$  mole fraction and  $\delta^{13}\text{C}$ - $\text{CH}_4$  data suggest that thermogenic sources are unlikely to be the dominant driver of the post-2006 global mean increase in atmospheric  $\text{CH}_4$  (Lan et al., 2021)). A growing body of work has proposed a range of hypotheses to explain short periods of observed global and regional variations in atmospheric  $\text{CH}_4$  (Turner et al., 2019). In this study, we take a step back to look at observed  $\text{CH}_4$  variations from 2004 to 2020, in order to capture the some of the zero-growth rate period and the subsequent increase in growth rate of  $\text{CH}_4$  post-2007. We argue that monthly variations are part of a large-scale shift ~~of predominately thermogenic energy emissions from high northern latitudes from predominately thermogenic emissions from northern midlatitudes~~ to biogenic emissions from the tropics, driven by ~~Tropical North African and Tropical South American wetlands~~ larger emissions over tropical North Africa and tropical South America.

The post-2007 increase in atmospheric  $\text{CH}_4$  has been the focus of many studies and has been attributed to different plausible hypotheses associated with changes in various emissions sources, and the OH sink (Turner et al., 2019). These studies have reached their conclusions using *in situ* mole fraction observations alone or in combination with other observations, e.g. *in situ*  $\delta^{13}\text{C}$  (Schaefer et al., 2016; Rice et al., 2016; Nisbet et al., 2016; Fujita et al., 2020; Lan et al., 2021; Basu et al., 2022), satellite observations (Worden et al., 2017; McNorton et al., 2018; Yin et al., 2021; Feng et al., 2022), or other trace gases, using a variety of analysis methods and computational models. Typical emissions sizes and uncertainty are indicated in Table 1, adapted from Saunio et al. (2020). Our approach is unique in that, for our  $\delta^{13}\text{C}$  inversion, we are solving for the  $\delta^{13}\text{C}$  isotopic source signature of a geographical region. From the isotopic source signature of a region, we can determine how the source

balance within a particular region has shifted over time (~~i.e., towards more pyrogenic, thermogenic or biogenic sources~~), and ~~so~~, e.g. larger or smaller contributions from pyrogenic and biogenic sources, and consequently gain understanding of the geographical shifts in the CH<sub>4</sub> budget.

~~The reaction with Methane oxidation by~~ the OH radical in the troposphere is ~~the largest sink of CH<sub>4</sub>~~, responsible for 80% of the total CH<sub>4</sub> sink globally. Changes in OH may have played a role in recent changes in atmospheric CH<sub>4</sub> (Rigby et al., 2017; Turner et al., 2017) but the magnitude of this influence is uncertain (its short atmospheric lifetime of <1 s makes direct measurement of global variability very difficult). Reducing values of OH effectively increases atmospheric CH<sub>4</sub> and therefore has the same effect as increasing emissions of CH<sub>4</sub>. Chemical reactions responsible for removing CH<sub>4</sub> from the atmosphere are faster for lighter isotopologues of CH<sub>4</sub>. This isotopic fractionation therefore leads to an atmosphere enriched in heavier isotopes relative to the globally emitted CH<sub>4</sub>. Lan et al. (2021) simulated CH<sub>4</sub> and δ<sup>13</sup>C in a 3-D chemistry transport model covering the period 1984–2016, and found that changes in OH proposed by ~~(Turner et al., 2017)~~ Turner et al. (2017) are not consistent with the trend of increasingly isotopically light δ<sup>13</sup>C observed in the atmospheric record. We explore the impact of reducing OH in a sensitivity study. ~~The first COVID-19 lockdown in~~, taking into account a larger OH decrease during 2020 corresponded to an unexpected large increase in atmospheric CH<sub>4</sub>. ~~Studies have suggested this could be partly explained by a 3–5% reduction in OH (Miyazaki et al., 2021; Laughner et al., 2021) resulting from a large-scale reduced emissions of nitrogen oxides associated with industry. This has yet to be corroborated by satellite data that provide complementary constraints on the key emitting regions over the tropics (Feng et al., 2022). (Peng et al., 2022; Feng et al., 2023) that was associated with widespread reductions in nitrogen oxide emissions (Cooper et al., 2022).~~

Here, we calculate trends in regional CH<sub>4</sub> emissions and isotopic δ<sup>13</sup>C source signatures across the world, ~~2004–2020~~ 2004–2020, using *in situ* mole fraction and δ<sup>13</sup>C data, and satellite column-averaged dry-air mole fraction data. This is achieved by using three sets of inversions: two Maximum A-Posteriori inversions using ground-based data (solving separately for regional emissions and isotopic sources signatures), and an Ensemble Kalman Filter inversion using GOSAT data (solving for regional CH<sub>4</sub> emissions).

In the next section, we describe the data and methods we use to quantify changes in regional CH<sub>4</sub> emissions and the corresponding regional stable isotope source signatures. In section 3, we report our results of *a posteriori* regional CH<sub>4</sub> fluxes and regional δ<sup>13</sup>C isotopic signatures, including analysis of sensitivity calculations that involve different assumptions about year to year changes in the OH sink. We conclude the paper in section 4.

## 2 Data and Methods

### 2.1 *In Situ* and Satellite Remote Measurements of Atmospheric Methane

We use surface-level flask data as constraints on both regional CH<sub>4</sub> emissions and δ<sup>13</sup>C regional CH<sub>4</sub> emissions isotopic source signatures. The CH<sub>4</sub> mole fraction data are taken from 31 National Oceanic and Atmosphere Administration – Global Monitoring Laboratory (NOAA-GML) sites around the world (Figure 1), version 2020-07 (Dlugokencky et al., 2020). The data are monthly mean values, averaged from discrete data as collected at each site, analysed at NOAA-ESRL in Boulder, Colorado,

and recorded to the NOAA 2004A standard scale (Dlugokencky et al., 2005). Up to August 2019, the analysis was performed using gas chromatography (Steele et al., 1987, Dlugokencky et al., 1994; Dlugokencky et al., 2005) and since August 2019, cavity ringdown spectroscopy has been used (Dlugokencky et al., 2020). We also include data from a site in Siberia, Karasevoe (KRS), which is monitored by the National Institute for Environment Studies (NIES). This site was included to maximise geographical coverage of *in situ* data. The CH<sub>4</sub> mole fraction measurements from this site are continuous, measuring from 65 m height, covering the period ~~2004-2020~~ 2004-2020 (Sasakawa et al., 2010). A scale factor of 0.997 is applied to the NIES data in order to bring it into line with the NOAA 2004A scale (Zhou et al., 2009). The site constitutes part of the Japan-Russia Siberia Tall Tower Inland Observation Network (JR-STATION).

$\delta^{13}\text{C}$  data are similarly monthly mean values, calculated from discrete flask samples at NOAA network sites, reported on the international carbon isotope scale VPDB (Vienna Pee Dee Belemnite). Isotope ratio ‘delta’ values represent the excess of a heavy, less abundant stable isotope (for  $\delta^{13}\text{C}$  values, carbon-13) over the light, most abundant stable isotope (carbon-12) in a sample, when compared to a standard. These measurements are useful as they are indicative of the source of the CH<sub>4</sub>: biogenic sources are dominated by isotopically lighter signatures and thermogenic sources are dominated by isotopically heavier signatures. For the NOAA network, isotopic analysis of  $\delta^{13}\text{C}$  was performed at the University of Colorado Institute of Arctic and Alpine Research Stable Isotope Laboratory (CU-INSTAAR). They follow an isotope ratio mass spectrometry approach (Miller, 2002; Vaughn et al., 2004). The geographical locations of *in situ* measurement sites are shown in Figure 1. These sites are a subset of the entire NOAA network’s capacity for measuring CH<sub>4</sub> mole fractions. The sites included in the inversion (both for CH<sub>4</sub> and  $\delta^{13}\text{C}$ ) are those that cover the entire period of the inversion (2004-2020) without significant periods of measurement breaks to ensure a consistent interpretation of trends without consideration of possible biases introduced through the inclusion or exclusion of specific sites.

We also estimate CH<sub>4</sub> fluxes for 2010-2020 from the Japanese Greenhouse gases Observing SATellite (GOSAT) that was launched in 2009. GOSAT is in a sun-synchronous orbit with an equatorial local overpass time of 13:30. Since launch, it has provided continuous global observations of dry-air atmospheric column-averaged CO<sub>2</sub> (XCO<sub>2</sub>) and CH<sub>4</sub> (XCH<sub>4</sub>), retrieved from shortwave infrared wavelengths that are most sensitive to changes in CH<sub>4</sub> and CO<sub>2</sub> in the lower troposphere (Parker et al., 2020). We use the latest (v9) proxy XCH<sub>4</sub>:XCO<sub>2</sub> retrievals that use spectral absorption features around the wavelength of 1.6  $\mu\text{m}$  (Parker et al., 2020, Palmer et al., 2021), because of the smaller bias and better global coverage than those provided by the full physics retrievals. Analyses show the precision of single proxy retrieval is about 0.72%, with a global bias of 0.2% (Parker et al., 2011, 2015, 2020). In our calculations, we assume a higher observation uncertainty of 1.2%, and deduct a globally uniform bias of 0.3% to obtain better *a posteriori* agreement with the independent ground-based XCH<sub>4</sub> data by the Total Carbon Column Observing Network (TCCON). These uncertainties are detailed in Feng et al. (2022). To anchor the constraints from the proxy XCH<sub>4</sub>:XCO<sub>2</sub> ratio (Fraser et al., 2014; Feng et al., 2017), we also assimilate the GLOBALVIEW CH<sub>4</sub> and CO<sub>2</sub> data (Schuldt et al., 2021), with assumed uncertainties of 0.5 ppm and 8 ppb for *in situ* measurements of CO<sub>2</sub> and CH<sub>4</sub>, respectively. GLOBALVIEW constitutes a combination of CH<sub>4</sub> data from ground-based data (both flask and continuous) and aircraft data, from 54 different laboratories, combined and published by NOAA-GML (Schuldt et al., 2021). Locations of the assimilated GLOBALVIEW CH<sub>4</sub> (sub) dataset are shown in Feng et al., 2022.

## 2.2 GEOS-Chem Atmospheric Chemistry and Transport Model

125 To relate CH<sub>4</sub> emissions to atmospheric CH<sub>4</sub> concentrations, we use v12.1 of the GEOS-Chem 3-D global chemical transport model (CTM) (Bey et al., 2001) at a horizontal resolution of 2° (latitude) by 2.5° (longitude) with 47 vertical levels from the surface to 80 km height, with meteorological data from the MERRA-2 meteorological reanalyses (Gelaro et al., 2017) from the NASA Global Modeling and Assimilation Office (GMAO).

Our *a priori* emissions include: 1) monthly EDGAR ~~v4.3.2 anthropogenic emissions (Janssens-Maenhout et al., 2019)~~ v6 anthropogenic emissions (Crippa et al., 2021) that accounts for emissions from oil and gas, coal, livestock, landfills, wastewater, rice, and other anthropogenic sources (including biofuel) from 2004 to 2018; 2) monthly GFED-4 biomass burning emissions (version 4.1; Randerson et al., 2017); and 3) monthly v1.0 WetCHARTs wetland emissions (Bloom et al., 2017). The Harvard-NASA Emissions Component (HEMCO) software within GEOS-Chem converts the emission inventories at their native horizontal resolution to the GEOS-Chem 2° × 2.5° resolution. Beyond the end of the emissions inventory, emissions are  
135 repeated yearly in *a priori* simulation.

Table 1 shows the  $\delta^{13}\text{C}$  ~~isotopic source~~ signatures for the source types included in our simulations. These are extracted as mean global values from Sherwood et al. (2017), which provide a database of global isotopic source signatures that are broken down into the same sectors as we employed in our simulations. However, individual source types show a wide range of source signatures, and this uncertainty is reflected in the assigned uncertainty given to the *a priori* source signatures in inversion  
140 (Section 2.3). ~~We~~ In the inversion, we differentiate between Arctic and tropical wetlands by applying a 10‰ isotopically lighter source signature to the Arctic source (Table 1), following Ganesan et al. (2018) who produced a global wetland source signature map based ~~upon~~ on published  $\delta^{13}\text{C}$  data. In GEOS-Chem, we simulate isotopologues separately (i.e. for  $\delta^{13}\text{C}$ ,  $^{12}\text{CH}_4$  and  $^{13}\text{CH}_4$ ), and then calculate  $\delta^{13}\text{C}$  values. The arithmetic underlying the conversion of isotope ratios to isotopologue emissions for input to the model are detailed in Appendix A.

145 We include the loss of atmospheric CH<sub>4</sub> from reaction with chlorine, soil uptake, and from oxidation by OH. We use monthly 3-D fields of OH, calculated using the full-chemistry version of GEOS-Chem, and monthly 3-D field of atomic chlorine (Sherwen et al., 2016). Stratospheric loss frequency fields are determined using the NASA GMI stratospheric model (Duncan et al., 2007). Estimates of the microbial consumption of CH<sub>4</sub> in soils is determined from Fung et al. (1991). The resulting atmospheric lifetime of ~~CH<sub>4</sub>~~ CH<sub>4</sub> against OH is ~~9.73 years, consistent with the observed methyl chloroform lifetime of 5.39 years. This~~ 9.77 years. The corresponding lifetime for methyl chloroform is 5.41 years, which is consistent with atmospheric observation of methyl chloroform. This lifetime also compares well with ~~multi-model simulations~~ multi-mode  
150 of 7.2-10.1-10.1 yrs. (Voulgarakis et al., 2013; Morgenstern et al., 2017) that reported global mean lifetimes of CH<sub>4</sub> that range 7.2-~~10.1-10.1~~ yrs. In our default model configuration, none of these loss processes include interannual variations.

To account for isotopic fractionation due to loss of CH<sub>4</sub> in the troposphere and stratosphere, we use published kinetic  
155 isotope effect values (KIEs). These values are employed to scale the reaction rate constants used in the simulations for  $^{12}\text{CH}_4$  and  $^{13}\text{CH}_4$  (Table A1). The OH and Cl sinks are handled in the hard coding of the model, whereas the soil sink is handled as a

negative emission in the HEMCO file. Therefore, for the soil sink, the KIE is directly applied as a scale factor in the HEMCO configuration file (Snober and Quay, 2000; Burkholder et al., 2019).

~~'Spinning up' is an important aspect of atmospheric modelling in order for simulated mole fractions to reach equilibrium. We spin-up the model by scaling a GEOS-Chem restart file (a file from a previous GEOS-Chem model run. The restart file is at 4x5 resolution, and originally represented 2012, but is spun up to represent 2004. The  $\delta^{13}\text{C}$  inversion uses a posteriori regional emissions from the containing a default realistic distribution of  $\text{CH}_4$  inversion as a starting point, with sectoral emissions scaled as detailed in Appendix A. We then run the model over the year 2004 sixty times using the across the atmosphere) to conditions near representative of the start of our analysis in January 2004. We then ran the model sixty times with repeating 2004 MERRA-2 meteorology and emissions (corresponding to approximately six times the chemical lifetime of e-folding lifetimes for  $\text{CH}_4$ . We find this is sufficient to allow mole fractions and isotope ratios to equilibrate (not shown)) to improve as far as possible the simulation of atmospheric gradients in  $\text{CH}_4$  in the initial conditions. We then ~~run~~ ran a single-year inversion for 2004 to optimise the  $\delta^{13}\text{C}$  isotope ratios and  $\text{CH}_4$  values concentrations relative to ground-based observations, following the inverse method detailed below. The  $\delta^{13}\text{C}$  inversion used the regional emissions estimate provided by the posteriori from the  $\text{CH}_4$  inversion as a starting point, with sectoral emissions scaled as detailed in Appendix A. The output of this short inversion is improved estimates of initial conditions for  $\delta^{13}\text{C}$  and  $\text{CH}_4$  2004 inversion is a final step in creation of the initial conditions, which serve as a starting point for the longer inversion that we report here (2004-2020). This restart file originally represented 2012, however it is spun up over 60 years to the point where it no longer resembles 2012 and will be representative of 2004, the starting point of the simulation. 2004- 2020).~~

For all our calculations, we sample GEOS-Chem at the grid box and local time that corresponds to the *in situ* and satellite remote sensing data. For the satellite data, we also apply scene-dependent averaging kernels to account for vertical structure. This approach allows us to directly compare the model with measurements. Regional trends are calculated by examining the grid boxes which correspond to encompassed by a given region on the global grid.

### 180 2.3 Inverse Methods

We use two inverse methods that reflect the volume and simplicity of the data being used. For *in situ* data we use the Maximum *A Posteriori* (MAP) inverse methods and for the more voluminous satellite data we use an ensemble Kalman filter (EnKF). For brevity, we include only the essential details about either method and refer the reader to dedicated papers.

We use the Siegel linear non-parametric estimates (Siegel, 1980) to fit a line to our *a posteriori*  $\text{CH}_4$  emissions. This method is less sensitive to outliers, e.g. El Niño, that would otherwise compromise the linear trend estimate (Palmer et al., 2021), and the resulting linear trend estimate has lower variables than simpler methods. We find Siegel trend estimates are similar to those estimated by the Theil-Sen estimator.

### 2.3.1 Maximum A Posteriori

To infer regional *a posteriori* CH<sub>4</sub> fluxes and regional δ<sup>13</sup>C emissions source signatures from the atmospheric measurements of CH<sub>4</sub>, we use the Maximum A Posteriori solution (MAP) inverse method (Rodgers, 2000). We solve for CH<sub>4</sub> fluxes and δ<sup>13</sup>C emissions signatures from 14 geographical regions (Figure 1). This method combines *a priori* knowledge and its uncertainty with the measurements and their uncertainties, and has been used in a number of studies, e.g., Fraser et al. (2014); McNorton et al. (2018).

The MAP solution and the associated *a posteriori* uncertainty is described as, respectively:

$$\mathbf{x}^a = \mathbf{x}^b + (\mathbf{H}^T \mathbf{B}^{-1} \mathbf{H} + \mathbf{R}^{-1})^{-1} \mathbf{H}^T \mathbf{B}^{-1} (\mathbf{y} - \mathbf{H} \mathbf{x}^b), \quad (1)$$

$$\mathbf{A} = (\mathbf{H}^T \mathbf{B}^{-1} \mathbf{H} + \mathbf{R}^{-1})^{-1}, \quad (2)$$

using the conventional-convention that lower-case and upper-case variables denote vectors and matrices, where-respectively. The  $\mathbf{x}$  denotes the state vector that describes the estimated quantities, which in this study includes monthly CH<sub>4</sub> fluxes and δ<sup>13</sup>C source signatures from regions across the world (Figure 1). Subscripts ‘a’ and ‘b’ denote *a posteriori* and *a priori* CH<sub>4</sub> fluxes, respectively, and superscripts ‘-1’ and ‘T’ denote matrix inverse and transpose operations, respectively. The measurement vector  $\mathbf{y}$  includes CH<sub>4</sub> mole fraction or δ<sup>13</sup>C data. The matrices  $\mathbf{B}$ ,  $\mathbf{A}$ , and  $\mathbf{R}$  denote the error covariances matrices for the *a priori*, *a posteriori*, and measurements, respectively.  $\mathbf{B}$  and  $\mathbf{R}$  are diagonal matrices. For  $\mathbf{B}$  we assume uncertainties of 50% of the regional CH<sub>4</sub> fluxes and 15‰ for the δ<sup>13</sup>C values, and for  $\mathbf{R}$  we assume 10 ppb for the mole fraction data and 0.1‰ for the isotope data. These uncertainties were based upon-on similar studies (Fraser et al., 2014; McNorton et al., 2016). We assume a model transport error of 12 ppb, following Feng et al. (2022).

The Jacobian matrix  $\mathbf{H}$  describes the sensitivity of the measurements to changes in the state vector, i.e.  $\partial \mathbf{y} / \partial \mathbf{x}$ . For the mole fraction CH<sub>4</sub> inversion, the Jacobian matrix describes the sensitivity of mole fractions in the model to changes in regional CH<sub>4</sub> emissions. We construct the matrix using a series of GEOS-Chem model runs. We systematically let each individual emitting region (described by the state vector) emit for one month while all other regions are emitting as normal. The individual regional source is then switched off (emissions set to zero) and the effect of this on the 3-D atmospheric distribution of CH<sub>4</sub> mole fractions is recorded over the following three months. The result of this test is recorded at the grid boxes that correspond to the location of the measurement sites. The resulting mole fractions therefore describe the sensitivity of a particular measurement site to changes in a specific regional source up to three months after emission. This is repeated for every month within the inversion timescale, for every region described in the state vector.

For the δ<sup>13</sup>C inversions, the ~~a-priori-simulation-uses-a-posteriori-regional-emissions-from-the-CH<sub>4</sub>-inversion-as-a-starting-point~~. ~~The-Jacobian-matrix-in-this-case~~ Jacobian matrix describes the sensitivity of modelled δ<sup>13</sup>C to changes in the regional isotopic source signatures. We construct the Jacobian as the difference between a control model calculation (using the CH<sub>4</sub> *a posteriori* regional emissions and mean source signature values from Sherwood et al. (2017)) and perturbed source signature model calculation for the whole study period (2004-2020). For the perturbed model calculation, we systematically perturb the isotopic source signature of each region (all of the sectors that are containing-contained geographically within a region) isotopically heavier by 20‰ for the period 2004-2020. The difference between the control and perturbed run in δ<sup>13</sup>C value

at the location of each measurement site is then divided by the value of  $\delta^{13}\text{C}$  perturbation for the region source signature, to understand the effect of changing a regions source signature ~~upon-on~~ the  $\delta^{13}\text{C}$  value recorded at each measurement site location. ~~Each individual regions' model calculation is spun up separately from the control model calculation in order to account for lagging in the model.~~

The output from the inversion are improved estimates of regional  $\text{CH}_4$  fluxes and  $\delta^{13}\text{C}$  source signatures. The model simulates the global atmosphere on a  $2^\circ \times 2.5^\circ$  horizontal grid. The *a posteriori* regional  $\text{CH}_4$  fluxes and isotopic source signatures are applied to the grid boxes in the model which correspond to a given region in an *a posteriori* simulation. ~~The a posteriori simulation is then used to compare with the in-situ data to ensure the quality of the a posteriori fit.~~

### 230 2.3.2 Ensemble Kalman Filter

We use an Ensemble Kalman Filter (EnKF) approach in performing the inversion using satellite data, because we cannot easily evaluate the necessary matrix operations associated with an analytic inversion. Here we use an ensemble of flux perturbation pulses to represent uncertainty in our *a priori* estimate for regional monthly  $\text{CH}_4$  fluxes. We subsequently use a global chemistry transport model (i.e., the GEOS-Chem v12) to track the transport and chemistry processes of the tagged emission pulses in the atmosphere, to project their spreads to the observation space. With the ensemble of *a priori* flux perturbations, and the simulated observation impacts, we use the Ensemble Transform Kalman Filter (ETKF) algorithm to numerically estimate the *a posteriori*  $\text{CH}_4$  fluxes and the associated uncertainties by optimally comparing the model simulation with observations (see Feng et al., 2017 for more details). To reduce the computational costs, mainly from tracking tagged emission pulses, we introduce a 4-month moving lag window for each assimilation step, because any observation has limited ability to distinguish between the signals emitted long (>4 months) before, from variations in the ambient background atmosphere (Feng et al., 2017). As a result, we are able to include a larger state vector, consisting of monthly scaling factors for 487 (476 land regions and 11 oceanic regions) regional  $\text{CH}_4$  (and  $\text{CO}_2$ ) pulse-like basis functions (Figure S1 in (Feng et al., 2022) [Feng et al. \(2022\)](#)). We define these land sub-regions by dividing the 11 TransCom-3 (Gurney et al., 2002) land regions into 42 to 56 nearly equal sub-regions, and use the 11 oceanic regions defined by the TransCom-3 experiment. Because of their smaller sizes, we have assumed a higher uncertainty percentage (60%) for *a priori* emissions than the MAP approach described above. We also include spatial correlation with a correlation length of ~~500km~~ [500 km](#) between the sub-regions.

### 2.4 Sensitivity of Results to Changes in Assumed OH Distributions

To examine the sensitivity of our results to changes in ~~assumed OH distributions~~ [the magnitude of OH](#), we run a single sensitivity run that is made up of two parts. First, we imposed a 0.5%/yr uniform decrease to our 3-D OH field from 2004 to 2019, ~~following similar trends proposed by Turner et al. (2017) (who proposed a consistent with the 7% reduction in OH, 2003-2016) and second, we uniformly decrease OH by 5% over 2003-2016 proposed by Turner et al. (2017). Second, we imposed a larger global-scale OH reduction of 1.5% in 2020 to describe estimated changes due to a global-scale reduction in emissions of based on recent studies (Miyazaki et al., 2021; Laughner et al., 2021) to describe a more abrupt change due to widespread reductions in nitrogen oxides ( $\text{NO}_x$ ) associated with the first COVID-19 lockdown Miyazaki et al. (2021); Laughner et al. (2021). It has~~



255 also been suggested that OH mole fractions may have actually increased during 2000–2016 due to increasing water vapour and  $\text{NO}_x$  in the tropics (Zhao et al., 2019), however considering the scenario under COVID-19 lockdowns in closing down manufacturing during the first Covid-19 lockdown (Cooper et al., 2022). Newer studies have suggested the OH reduction in 2020, a decreasing trend over the previous years is only considered here. A similar approach to this was followed by Feng et al. (2022) for which there is some opposition that suggests the change in OH during COVID-19 should be larger, although there is no empirical determination of this change. We then recalculate was closer to 1% (Peng et al., 2022; Feng et al., 2023) but these estimates are also subject to uncertainties. The purpose of this numerical experiment is to determine the sensitivity of *a posteriori*  $\text{CH}_4$  flux estimates to changes in assumed variations in OH and not to determine a distribution of OH that simultaneously fits observed changes in  $\text{CH}_4$  and  $\delta^{13}\text{C}-\text{CH}_4$ .

### 3 Results

265 Here, we report *a posteriori* estimates for total  $\text{CH}_4$  emissions inferred from the ground-based data, *in situ* and GOSAT data and then the corresponding *a posteriori* isotopic source signatures for  $\delta^{13}\text{C}$ . We draw comparisons with previous studies throughout this section.

## 4 Results

### *A posteriori* emission estimates of total $\text{CH}_4$

270 Figure 2 shows the annual mean differences in regions between *a priori* emission estimates and *a posteriori* emission estimates for both ground-based (2004–2020) and GOSAT results (absolute 2009–2020). Absolute emissions values are plotted in Figure 3). This indicates the changes from the for completeness.

On a global scale, terrestrial *a priori*/*a posteriori* emissions and allows comparison of the two independent approaches. The inferred from *in situ* and GOSAT data have progressively increased relative to *a priori* emissions are constructed as detailed in Section 2.2. Focusing on values since about 2014. The peak difference is in 2020 (due to interest in emissions changes as a result of the COVID-19 lockdowns) on a global scale, when we find increased emissions relative to *a priori* emissions of  $72.0 \pm 68.5 \pm 35.5 \pm 61.5$  Tg/yr in 2020 for the *in situ* inversion and  $61.5 \pm 37.3$  Tg/yr higher emissions for the GOSAT inversion. The Global ocean  $\text{CH}_4$  emissions inferred from *in situ* inversion results indicate that this difference originates from tropical regions such as Tropical South America ( $+13.5 \pm 1.9$  and GOSAT data support a small negative bias ( $-1.2$  Tg/yr) in the *a priori*, which we do not discuss further.

280 As a zeroth order check of our *a posteriori* emission estimate of total  $\text{CH}_4$ , we compare in Figure 4 the published NOAA atmospheric growth rate of  $\text{CH}_4$  with our corresponding *a posteriori* atmospheric mole fractions. Generally, we find the *a posteriori* values inferred from *in situ* and GOSAT data are consistent with the overall trend of the changes in the growth rate, with large year-to-year changes that we explain now in terms of regional emission changes.

285 Changes in the global terrestrial emissions reflects changes from different geographical regions. Differences between *a posteriori*  
emission estimates inferred from *in situ* and GOSAT data are partly due to differences in the geographic coverage of the  
datasets. Ground-based data have poorer geographic coverage, particularly over the tropics and the southern hemisphere and  
satellite data are currently available at most once per day in cloud-free conditions. Using the *in situ* data, we find that the  
largest *a posteriori* emission increases over the 2004 to 2020, determined by the Siegel linear estimator, are over the tropics  
290 (3.6 Tg/yr in 2020), North Africa (+15.1 ± 6.8 /yr, comprising North Africa, tropical South America, and Tropical Asia),  
followed by China (1.6 Tg/yr, 2020) and China (+17.3 ± 4.4 /yr) then by small contributions (individually <0.2 Tg/yr, 2020).  
There are decreases relative to) from elsewhere. Table 1 provides an overview our annual mean sector-based *a priori* *posteriori*  
emissions in 2020 in Temperate North America (-13.3 ± 3.4 for 2004–2020. Generally, our values are close to the reported  
median values and within the range of values reported by Saunio et al. (2020).

295 Over the tropics, there is broad consistency between GOSAT and *in situ* data (Figure 2) that highlights the negative bias in  
the *a priori* over Northern Africa (bias of -8.6 Tg/yr), Southern Africa (-5.6 ± 2.1 Tropical Asia (bias of -7.2 Tg/yr), Temperate  
and Tropical South America (-4.1 ± 4.0 bias of -11.63 Tg/yr) and Boreal Eurasia (-2.3 ± 3.9. The *in situ* and GOSAT data for  
China support a small, steady increase in emissions from 2009 to 2020 (1.0 Tg/yr). According to these results, mid-latitude  
emissions are being overestimated and tropical emissions underestimated.

300 Likewise, the GOSAT-based inversion results indicate, with emissions inferred from the GOSAT data generally smaller than  
*a posteriori* *a priori* emissions increases from the values throughout the period (Figure 2). Data over India have a small mean  
annual trend (0.33 Tg/yr) over the same period. *a priori* *In situ* emissions are centred around tropical regions. In 2020, there are  
emissions increases from and GOSAT data are more consistent in sign (but not magnitude) at temperate latitudes (Figure 2).  
*A posteriori* emissions from *in situ* and GOSAT data are generally lower than the *a priori* estimates in Tropical South America  
305 (+20.3 ± 1.9 by more than 12.0 Tg/yr ) and North Africa (+13.1 ± 6.8 and 5.6 Tg/yr). Similar to the *in situ* results, there are  
decreases in some mid-latitude regions, specifically, respectively, over Temperate North America (-3.9 ± 1.8, and higher  
by more than 13.0 Tg/yr ) and Temperate South America (-6.4 ± 7.1 and 7.0 Tg/yr, respectively, over Temperate Eurasia, with  
the smallest discrepancies relative to the *a priori* before 2009. *A posteriori* emissions from boreal regions appear to be larger  
than *a priori* values by 4.2 Tg/yr )

310 The increase in tropical emissions has been highlighted by previous studies, whether using GOSAT data or before 2009  
(Figure 2). After 2009, *in situ* data as constraints in a 3-D CTM inversion (McNorton et al., 2016 and Fujita et al., 2020,  
examining (2003-2015) and (1995-2013) respectively). The increase in North Africa is especially noteworthy in 2020, where  
emissions have been attributed to increased wetland emissions by previous studies (Lunt et al., 2019, 2021; Pandey et al., 2021; Feng et al.,  
)

315 There are some differences between the two inversion results, likely due to the differing geographic coverage of the different  
datasets (ground-based data has poorer geographic coverage, and satellite data are available only once per day in cloud-free  
conditions). Specifically, emissions from Boreal North America and China are lower than the become progressively more  
consistent with the *a priori* over North America and is typically smaller than *a priori* values over Eurasia by 2.6 Tg/yr. For  
GOSAT, we find the converse situation: after 2009, data are lower than *a priori* emissions for the GOSAT-based inversion

320 ~~( $-4.6 \pm 1.1$  and  $-5.1 \pm 3.8$  values by  $4.4$  Tg/yr in 2020 respectively), but increase for the over North America and comparable~~  
~~with a priori values over Eurasia. In the southern hemisphere, in situ data closely a priori values, as expected, since there are~~  
~~fewer places where in situ inversion ( $+4.4 \pm 3.6$  and  $+17.3 \pm 4.4$  data are collected. GOSAT data show a small but persistent~~  
~~increase in emissions with time over Southern Africa ( $0.41$  Tg/yr in 2020 respectively). It is noteworthy that, despite differences~~  
~~in the absolute annual emissions estimates, both the GOSAT-based inversion and), highlighting the negative bias in a priori~~  
325 ~~emissions over Australia and over Temperature South America.~~

We use the a posteriori error covariance matrix from our MAP inversion (A, equation 2) to determine our ability to  
independently estimate CH<sub>4</sub> emissions from our geographical regions. Figure A1 shows no significant a posteriori correlations  
between neighbouring geographical regions in our state vector. This is consistent with the in situ based inversion indicate  
a gradual emissions increase in China from 2012. Sheng et al. (2021) find data being able to estimate independently regional  
330 ~~emission estimates in our state vector.~~

Our a posteriori emission estimates are broadly consistent with previous studies. For example, the increase in tropical  
emissions has been reported using GOSAT data or in situ data within a 3-D CTM inversion (McNorton et al., 2016; Fujita et al., 2020)  
, which examined shorter time periods of 2003–2015 and 1995–2013, respectively. The increase over Eastern Africa (that lies  
within our North Africa region) has been reported by several studies (Lunt et al., 2019, 2021; Pandey et al., 2021; Feng et al., 2022, 2023)  
335 ~~Sheng et al. (2021) reported using GOSAT data that CH<sub>4</sub> emissions from China increasing-increased by  $0.36$  Tg/yr, from~~  
~~2012 to 2017 using GOSAT data. Comparing 2017. Over the same time period, we find-estimate an increase of Chinese~~  
~~emissions of  $0.63$ – $0.64$  Tg/yr inferred from the ground-based and  $0.50$  Tg/yr inferred from in situ data and increase of  $0.50$~~   
~~Tg/yr inferred from the GOSAT data. We find that China has an isotopically lighter  $\delta^{13}\text{C}$  source signature from 2012 (Figure 5),~~  
~~similar to the other regions we study, however the isotopic shift in the latitude band that corresponds to China is not as large as~~  
340 ~~in others (Figure ??), which suggests that heavier isotopic signature sources (such as coal mines) could be part of the emissions~~  
~~makeup here.~~

~~We see improved emissions estimates for and GOSAT data, respectively.~~

Figure A2 shows observed CH<sub>4</sub> timeseries at ground-based sites that we use to determine the corresponding GEOS-Chem  
a posteriori versus a priori simulations. Figure A2 shows mole fraction estimates and a posteriori mole fraction estimates  
345 ~~inferred from ground-based data at site locations. We find smaller residuals between simulated mole fractions using the fractions,~~  
~~a posteriori a priori emissions and the measurements values already show excellent agreement with observations (mean resid-~~  
~~ual  $9.01$  ppb; of  $14.1$  ppb and root-mean-square error (RMSE)  $11.94$  ppb) than between the of  $18.3$  ppb), but this is generally~~  
~~improved after the model is fitted to the a priori in situ values and the measurements (mean residual  $13.06$  ppb; RMSE  $17.13$~~   
~~data, with smaller mean residuals ( $12.5$  ppb) and RMSE ( $17.0$  ppb). This compares favourably with is consistent previous~~  
350 ~~studies such as McNorton et al. (2018), with that reported a posteriori RMSE of  $12.30$  ppb. Likewise, we see agreement of~~  
~~mole fraction estimates using GOSAT data (Figure A4; mean residual  $41.72$  ppb, RMSE  $51.57$  ppb). There are no significant~~  
~~values of  $12.3$  ppb. Figure A3 shows a posteriori correlations between neighbouring regions (Figure A1), determined by the~~  
~~CH<sub>4</sub> mole fractions at NOAA sites that we do not include the inversion. This provides an additional and independent test of~~  
~~our ability to describe atmospheric CH<sub>4</sub> using a subset of NOAA data that we use in our inversion (Table A2). Generally,~~

355 ~~our a posteriori error covariance matrix, A, meaning that estimates agree with these independent data, but for some sites the~~  
~~model has difficulty reproducing the data, e.g. AMY (western S. Korea), KZD (Kazakhstan), and SDZ (mainland China). This~~  
~~is because some sites are influenced by local sources that are not representative of the spatial scale of our transport model~~  
~~( $\approx 50,000$  km<sup>2</sup>). Similarly, we find agreement using a posteriori regional emissions estimates are independent of one another.~~  
360 ~~Independent validation of the a posteriori mole fractions are provided by comparison with NOAA network sites not included~~  
~~in the inversion using GOSAT data (Figure A3A4; mean residual of 29.1 ppb and RMSE 35.1 ppb).~~

### A posteriori source signatures of $\delta^{13}\text{C}$

Figure 5 shows a posteriori regional  $\delta^{13}\text{C}$  emissions source signatures inferred from ground-based *in situ* data. ~~The results are~~  
~~grouped. We group our results~~ into approximately three-year bands, as a residual from the ~~2004-2007~~ 2004-2007 mean value,  
to show how the regional isotopic source signatures change across the time series.

365 Relative to a priori emissions (Figure A5), a posteriori values from Northern Boreal regions (Boreal North America and  
Eurasia) have isotopically lighter signatures ( $-62\text{‰}$ ) ~~;- consistent with the dominance of biogenic emissions due to a larger~~  
~~contribution from isotopically lighter biogenic emissions and/or a smaller contribution from isotopically heavier thermogenic~~  
~~or pyrogenic emissions~~ (Figure A5). Conversely, a posteriori values from regions such as Temperate Eurasia, Australia and  
Southern Africa have isotopically heavier source signatures (approximately  $-40\text{‰}$ ) ~~;- suggesting a greater due to a larger pro-~~  
370 ~~portion of thermogenic or pyrogenic emissions -and/or a smaller contribution from isotopically light biogenic emissions.~~

Figure 5 shows a general trend towards isotopically lighter regional source signatures of  $\delta^{13}\text{C}$  across the time series. ~~This~~  
~~Our analysis suggests this~~ trend has been ongoing since 2012 and is observed in all regions worldwide, ~~however is strongest as~~  
~~but is strongest~~ (compared with a priori estimates ~~in~~) ~~over~~ Tropical and Southern Hemispheric regions ~~such as~~. ~~For example,~~  
Tropical South America and Southern Africa ~~( $-1.8\text{‰}$  and  $-2.1\text{‰}$  are  $1.2\text{‰}$  and  $0.9\text{‰}$  isotopically lighter than a priori values for~~  
375 ~~for 2019 and 2020, respectively). Emissions from these tropical regions have a strong  $\delta^{13}\text{C}$  seasonal cycle (Figure A5), with~~  
~~isotopically lighter values during summer months, driven by a greater proportion of biogenic emissions at this time. It therefore~~  
~~follows that less significant seasonality is indicative of thermogenic or pyrogenic emissions making up a significant part of the~~  
~~emissions mix (observed for example in China and Temperate Eurasia). There is also evidence to suggest a period around 2012~~

380 ~~Our analysis also highlights a period 2007-2012~~ when regional source signatures, ~~particularly northern hemisphere regions,~~  
become isotopically heavier ~~(by approximately  $-1.0\text{‰}$  compared with a priori source signatures )~~ ~~;- especially in the Northern~~  
~~Hemisphere, before becoming isotopically lighter again. This suggests a~~ (by  $1.0\text{‰}$  2007-2009; by  $0.8\text{‰}$  2010-2012; and  $0.3\text{‰}$   
2013-2015). After 2012, regional source signatures of  $\delta^{13}\text{C}$  generally become isotopically lighter. This result is suggestive that  
2012 was a period when there was a change in the sources of balance of global sources that determine changes in atmospheric  
385 ~~CH<sub>4</sub> dominating CH<sub>4</sub> emissions during this brief period.~~ These isotopic shifts in 2008 and 2012 are noted by Nisbet et al.  
(2016), who ~~use~~ used a box model and examine data from sites measured by NOAA and Royal Holloway, University of  
London (RHUL). They found that changes in removal rates ~~would~~ could not explain these anomalies ~~;- the events are therefore~~  
so that these events were attributed to changing emissions.

~~We find some significant~~ We find that China experiences a weaker shift in 2012 to a (0.1‰) isotopically lighter  $\delta^{13}\text{C}$  source signature compared to a *posteriori* ~~priori~~ correlations between neighbouring regions for these values (Figure 5) and compared to other temperate regions. This suggests that heavier isotopic source signatures (Figure A6), ~~determined by such as coal mines~~ play a larger contribution to this region.

Unlike the *a posteriori* ~~error-covariance matrix~~, total  $\text{CH}_4$  emission estimates, we find significant *Aa posteriori* ~~, which indicates that we cannot differentiate between the isotopic source signatures of neighbouring regions (such as correlations~~ between neighbouring regions for  $\delta^{13}\text{C}$  source signatures (Figure A6). For example, there is a correlation of 0.95 between estimates for Southern Africa and Temperate South America ~~). This so these cannot be considered as independent estimates. This result~~ aligns with Basu et al. (2022) ~~, who used both who used~~  $\text{CH}_4$  mole fraction and  $\delta^{13}\text{C}$  measurements to determine that tropical biogenic sources are driving  $\text{CH}_4$  growth, ~~however acknowledge. They acknowledged~~ that measurement coverage ~~limits possible conclusions based upon limited conclusions based exclusively on~~ isotope ratio measurements. Nevertheless, ~~the~~ they found a clear trend of stronger emissions of isotopically lighter  $\text{CH}_4$  ~~is clear, indicating, indicative of~~ an increased role ~~in~~ for biogenic emissions in the global source makeup.

~~The corresponding~~ We find that *a posteriori* regional  $\delta^{13}\text{C}$  source signatures ~~produce an atmospheric time series result in a time series of  $\delta^{13}\text{C}$  that is~~ more consistent with ~~measurements-observations~~ than *a priori* values (Figure A7), ~~particularly during 2008-2018 as expected. This particularly affects the period 2008-2018~~ when *a priori* emissions source signatures are ~~significantly~~ isotopically lighter. Figure A7 shows  $\delta^{13}\text{C}$  ~~Our a priori and a posteriori values at site locations. The a posteriori source signatures result in smaller residuals between the a posteriori simulation and measurements (mean residual a mean observed-model residual and RMSE of 0.11‰, RMSE 0.15‰), than from the prior (mean residual 0.19‰, RMSE 0.23‰). This result compares well to McNorton et al. (2018) (and 0.14‰, respectively. These are smaller than those corresponding to a posteriori a priori values for the observed-model residual (0.37‰) and RMSE (0.41‰). Our comparison is consistent with McNorton et al. (2018) (RMSE 0.1‰) and Fujita et al. (2020) (a posteriori RMSE 0.08-0.25‰).~~

In Figure ??, we combine this information into a zonal plot, reported approximately every 30 latitude, for  $\text{CH}_4$  emissions and the corresponding changes in regional isotopic source signatures of  $\delta^{13}\text{C}$ . We find consistency between the magnitude of the changes in  $\text{CH}_4$  inferred from ground-based and GOSAT data, particularly in the low latitudes. The plot also shows there has been a progressive increase in emissions from tropical latitudes (between 60-80 Tg

## 415 Sensitivity to assumptions about OH

Figure 6 shows the result from our sensitivity test that assumes 0.5%/yr in 2019-2020) and a decrease at northern midlatitudes (up to -10 Tg/yr). This suggests that emissions have shifted from northern midlatitudes towards tropical emissions. We also find a move towards isotopically lighter regional source signatures of  $\delta^{13}\text{C}$  across all latitudinal bands, with a change of approximately -2‰ in the tropics. Comparing Figures 5 and ??, we see similar trends across latitudinal bands and the regions within them, for example trends in European and Chinese source signatures align with the 30-60N latitudinal band. Our results compare well with Nisbet et al. (2019), who use a box model to fit emissions scenarios to in situ measurements, examining

2000–2018. They show strongest emissions increases from the tropics (approximately +20 Tg/yr, Figure 5). They likewise show consistently isotopically lighter atmospheric  $\delta^{13}\text{C}$  across the time series, by approximately 0.03%/yr.

425 Figure 4 compares our calculated atmospheric growth rate from the model simulations with the growth rates calculated from the in situ observations alone. We applied the same technique as NOAA follow to compare their published growth rate to the a posteriori mole fractions of our inversion. The general trend in increasing growth rate is evident in both measurement and model datasets with inter-annual discrepancies explained through model-measurement mismatch at specific sites. uniform decrease to our 3-D OH field from 2004 to 2019, followed by a more abrupt decrease of -1.5% in 2020 to describe the widespread reduction in nitrogen oxide emissions. This is an idealised sensitivity test that is inconsistent with global-scale  
430 constraints on estimates of the global mean atmospheric growth of atmospheric CH<sub>4</sub>, i.e., most of the observed global growth in atmospheric CH<sub>4</sub> can be explained by the changes in OH. Nevertheless this test provides us with some idea of the robustness of our results against changes in OH.

Figure 6 shows that the ~~0.5% negative trend in~~ We find that this alternative assumption about OH does not make a significant difference to our significantly affect our results until much later in the timeseries (2017–2019), reflecting our large *a posteriori* estimates (emissions change is not larger than uncertainties. We find a similar quality of fit of the *a posteriori* uncertainty) until later in the timeseries (2017–2019), reflecting our large model to the data with or without considering the OH trend (not shown). This does not preclude a role for changes in OH but the concurrent *a posteriori* uncertainties. However, we find that a sudden 5% decrease in OH during shifts in CH<sub>4</sub> emissions and regional isotopic source signatures of  $\delta^{13}\text{C}$  are consistent with decreasing OH playing a smaller role than increasing emissions of isotopically light  $\delta^{13}\text{C}$  source signatures in determining  
440 observed changes in atmospheric CH<sub>4</sub> (Lan et al., 2021).

The larger, abrupt change in 2020 results in a marked reduction (approximately ~~9%, 50–6%, 40~~ Tg/yr) in the emissions necessary to explain the increase in atmospheric CH<sub>4</sub>. ~~This reduction in emissions increases particularly affects high-emitting regions such as China and Tropical Asia. Despite this, the regional results are generally within the~~ There is still debate about the impact of a posteriori uncertainties of our control calculation, which does not include a year-to-year change in OH. On balance,  
445 given the large-scale, unprecedented changes in atmospheric chemistry during 2020 it is likely that OH has played a role in the global atmospheric growth rate of CH<sub>4</sub>, but changes in emissions likely overwhelm the impact from reduced OH methane emissions. Peng et al. (2022) used in situ data and concluded that the increase in atmospheric CH<sub>4</sub> in 2020 could be attributed approximately equally between a decrease in OH and an increase in OH. Analysis of GOSAT suggest that increased emissions play a larger role (Qu et al., 2022; Feng et al., 2023). We find a similar fit of the model to data with or without considering the  
450 OH trend (not shown).

## 4 Conclusions

We estimated regional CH<sub>4</sub> emissions and  $\delta^{13}\text{C}$  source signatures for the period ~~2004–2020~~ 2004–2020, inclusively, by fitting the GEOS-Chem 3-D atmospheric chemistry transport model to surface mole fraction data and GOSAT atmospheric column data using Bayesian inverse methods. Collectively, our results indicate that the post-2007 increases in CH<sub>4</sub> emissions are best

455 explained by a progressive latitudinal shift in emissions from the northern midlatitudes to tropical latitudes. *A posteriori* CH<sub>4</sub> emission estimates inferred from the ground-based and GOSAT data show larger tropical emissions, particularly over North Africa, Tropical Asia, and Tropical South America, and over China and at the same time as mid-latitudinal emission ~~proportion~~ proportions decreases. Source signature estimates inferred from the  $\delta^{13}\text{C}$  measurements over the same time period indicate that the latitudinal shift in CH<sub>4</sub> emissions is due to larger proportion of ~~biogenic sources~~ sources with a lighter atmospheric  
460  $\delta^{13}\text{C}$  signature (e.g., biogenic source such as wetlands) and/or a smaller proportion of sources with a heavier atmospheric  $\delta^{13}\text{C}$  signature (e.g., thermogenic or pyrogenic sources). Our results are broadly consistent with previous studies that focus on shorter, contributing periods (McNorton et al., 2018; Nisbet et al., 2019; Fujita et al., 2020; Yin et al., 2021; Lan et al., 2021; Basu et al., 2022)).

~~Our control calculations used monthly 3-D distributions of OH without any year-to-year variation. To explore how changes~~  
465 ~~in OH might affect our results, we ran a sensitivity experiment for which the monthly 3-D OH fields was decreased. We find that~~ our main results are robust against assuming a 0.5%/yr OH decrease from 2004 to 2019, inclusively, based on values proposed  
~~by previous studies (Turner et al., 2017). For this sensitivity experiment, we find our results are within a posteriori uncertainty~~ of the control calculations for most of the time series, and therefore steadily decreasing OH concentrations are not responsible  
~~for observed changes in the distribution of CH<sub>4</sub>. We also considered how a proposed larger 5% change in~~ consistent with  
470 Turner et al. (2017), followed by an abrupt 1.5% OH drop in 2020 (Miyazaki et al., 2021; Laughner et al., 2021), due to widespread  
~~COVID-19 related emission reductions in nitrogen oxides, affected our results. We find smaller CH<sub>4</sub> emissions increases during~~ 2020, as expected, but for most regions they are still within our control a posteriori emissions estimates for 2020. A much larger  
~~reduction in OH would be necessary to describe exclusively observed changes in atmospheric CH<sub>4</sub>, which would consequently~~ affect regional isotope signatures and observed variations of many atmospheric trace gases in a manner that has yet to be  
475 reported that reflects the widespread decrease in nitrogen oxide emissions from shutting down manufacturing during the first  
Covid-19 lockdown. This is an idealised sensitivity test but nevertheless provides us with some idea of the robustness of our  
results against changes in OH.

Sparse geographic coverage of ground-based data results in larger uncertainties for regional emission estimates that are ~~poorly covered~~ informed by fewer data, i.e. ~~high and low latitudes~~ in both hemispheres. For CH<sub>4</sub>, this deficiency can be partly  
480 addressed using the satellite data, but isotope ratios cannot usefully be retrieved from Earth observation satellite instruments.  
~~In this study,~~ We use only three measurement sites for  $\delta^{13}\text{C}$  in the Southern Hemisphere, which have a continuous record over the period of study. A consequence of this data ~~sparseness~~ sparsity is strong correlations between source signatures from neighbouring regions (Figure A6). ~~We further limited our study by picking measurements sites for which data are available over our study period (Figure 1). Sectoral~~ We assume mean sectoral  $\delta^{13}\text{C}$  source signatures ~~are taken as mean values~~ from  
485 Sherwood et al. (2017). These values are highly uncertain, as different sectors produce a range of possible  $\delta^{13}\text{C}$  values, and there are significant overlaps between recorded source signatures (Douglas et al., 2017), but the values chosen represent our current best knowledge of mean values. These data have greater value when they are used in a broader context with other data, as we have described in this study. We have used satellite observations to help identify that large-scale emission changes over regions that coincide with wetlands. ~~The collective evidence demonstrates that increasing tropical wetland emissions play~~

490 Collectively, empirical evidence, including *in situ* and GOSAT observation of CH<sub>4</sub> and *in situ* δ<sup>13</sup>C data, points to an  
increasing biogenic source originating from the tropics. While we cannot definitely attribute these changes to increasing  
wetland emissions, there is sufficient contextual evidence, building on previous studies, to suggest that wetlands are playing  
a significant role in ~~the observed atmospheric growth~~ recent growth of atmospheric CH<sub>4</sub>. First, large changes in OH that  
would needed to explain this atmospheric growth are inconsistent with increasingly isotopically light δ<sup>13</sup>C observations in  
495 the atmospheric record (Lan et al., 2021). Second, we know from *in situ* data the broad geographical regions responsible for  
increasing CH<sub>4</sub> emissions and isotopically lighter δ<sup>13</sup>C source signature, where the seasonal cycles are consistent with biogenic  
emissions peaking outside the burning season. Third, GOSAT provide us with additional information about the geographical  
distribution of CH<sub>4</sub> emissions: tropical emission hotspots are collocated with known wetland regions (Lunt et al., 2019, 2021; Pandey et al.  
. Finally, we also have evidence from other satellite data, e.g., hydrology, that help explain the growth of wetland emissions  
500 in the last decade (Lunt et al., 2019; Feng et al., 2022). Greater confidence in source attribution of changes in atmospheric  
CH<sub>4</sub> may come from collecting and interpreting δD and multiply-substituted ‘clumped’ isotopes (Douglas et al., 2017; Chung  
and Arnold, 2021), alongside δ<sup>13</sup>C. This needs to be accompanied by field measurements of these isotope ratios to improve  
delineation between different sectors.

~~Our work is also consistent with recent studies that have reported anomalous large CH<sub>4</sub> emissions over Eastern Africa (East~~  
505 ~~Africa and the Horn of Africa) due to elevated rainfall over upstream catchment areas (Lunt et al., 2019, 2021; Pandey et al., 2021)~~  
~~. These large-scale precipitation changes have been linked with the positive phase of the Indian Ocean Dipole (Feng et al., 2022)~~  
~~, which describes a sea-surface temperature gradient over the Indian Ocean. Similarly, increased CH<sub>4</sub> emissions over the~~  
~~Amazon basin (Wilson et al., 2021) are linked with large-scale changes in climate (Feng et al., 2022). These substantial increases~~  
The evidence presented here is consistent with a growing body of work that points to a substantial increase in biogenic CH<sub>4</sub>  
510 emissions from the tropics. This increase will likely have major implications for our achieving the goals of the Paris Agree-  
ment (Nisbet et al., 2019). Nature does not care about the origin of atmospheric CH<sub>4</sub> so that increasing biogenic emissions will  
require larger emission reductions from anthropogenic sectors, placing additional pressure on citizens to reduce their carbon  
footprints.

## 5 Code and data availability

515 The community-led GEOS-Chem model of atmospheric chemistry and model is maintained centrally by Harvard University  
(<http://geos-chem.seas.harvard.edu>), and is available on request. The ensemble Kalman filter code is publicly available as  
PyOSSE (<https://www.nceo.ac.uk/data-tools/atmospheric-tools/>).

## 6 Data availability

All the data and materials used in this study are freely available. The NOAA-GML and CU-INSTAAR ground-based CH<sub>4</sub> and  
520 δ<sup>13</sup>C data are available from the NOAA GML FTP server (<https://gml.noaa.gov/dv/data>), subject to their fair use policies. Data



from JR-STATION network was provided with cooperation of NIES Japan. The University of Leicester GOSAT Proxy v9.0 XCH<sub>4</sub> data are available from the Centre for Environmental Data Analysis data repository at (<https://doi.org/10.5285/18ef8247f52a4cb6a14013f8235cc1eb>), and from the Copernicus Climate Data Store. EDGAR data is available at (<https://edgar.jrc.ec.europa.eu/>), GFED-4 data is available at (<https://www.globalfiredata.org/data.html>), WETCHARTS data is available at ([https://daac.ornl.gov/cgi-bin/dsvviewer.pl?ds\\_id=1502](https://daac.ornl.gov/cgi-bin/dsvviewer.pl?ds_id=1502)).

## Appendix A: Isotologue Emissions

To simulate the atmospheric isotope ratio  $\delta^{13}\text{C}$  the isotologues  $^{12}\text{CH}_4$  and  $^{13}\text{CH}_4$  are considered separately in the model. To calculate the specific sectoral isotologue emissions we use the emissions calculated from the mole fraction CH<sub>4</sub> simulation and the isotope ratios defined in Table 1. We consider the isotope  $^{13}\text{C}$  relative to all isotopes in the sample (designated thereafter as  $13x$ ) using:

$$13x = \frac{^{13}\text{C}}{^{12}\text{C} + ^{13}\text{C}} = \frac{^{13}\text{C}/^{12}\text{C}}{1 + (^{13}\text{C}/^{12}\text{C})}, \quad (\text{A1})$$

where  $^{13}\text{C}/^{12}\text{C}$  is calculated from the  $\delta^{13}\text{C}$  reported on the international carbon isotope scale VPDB (Vienna Pee Dee Belemnite). This is the proportional molar abundance of the isotologues containing  $^{13}\text{C}$  (dominated by  $^{13}\text{CH}_4$ ) relative to the isotologues containing  $^{12}\text{C}$  (dominated by  $^{12}\text{CH}_4$ ). This value has to be adjusted before being applied in GEOS-Chem to convert from isotope ratio values to kg values used by emission inventories:

$$SF13 = 13x \times \frac{M_{13}}{M_{tot}}, \quad (\text{A2})$$

where  $SF13$  is the scale factor applied to each emissions type for the  $^{13}\text{CH}_4$  simulation,  $M_{13}$  is the molecular weight of  $^{13}\text{CH}_4$  (17.035 g/mol) and  $M_{tot}$  is the molecular weight of CH<sub>4</sub> (16.04 g/mol).

For the  $^{12}\text{CH}_4$  counterpart to  $^{13}\text{CH}_4$ , we use a similar approach. The ratio of  $^{12}\text{C}$  compared with all isotopes in the sample (designated as  $12x$ ) is given by:

$$12x = \frac{^{12}\text{C}}{^{13}\text{C} + ^{12}\text{C}}. \quad (\text{A3})$$

This is similarly adjusted from molar to mass ratio;  $SF12$  is the scale factor for each emissions type in the  $^{12}\text{CH}_4$  simulations:

$$SF12 = 12x \times \frac{M_{12}}{M_{tot}}, \quad (\text{A4})$$

where  $M_{12}$  is the molecular weight of  $^{12}\text{CH}_4$  (16.03 g/mol). Since  $^{13}\text{C}$  and  $^{12}\text{C}$  are the only stable carbon isotopes of CH<sub>4</sub>,  $13x$  and  $12x$  should sum to 1.

*Author contributions.* A.D. led the data analysis with contributions from P.I.P. and L.F. A.D. and P.I.P. led the writing of the paper with contributions from L.F. and T.A.. X.L., S.M., R.P. and H.M. provided data.

*Competing interests.* The authors declare that they have no competing interests.

550 *Acknowledgements.* A.D. is supported by the University of Edinburgh's E3 Doctoral Training Partnership, funded by the ~~National~~Natural  
Environment Research Council. P.I.P., L.F. and R.P. acknowledge support from the UK National Centre for Earth Observation funded by  
the ~~National~~Natural Environment Research Council (NE/R016518/1 and NE/N018079/1) and the Copernicus Climate Change Service  
(C3S2\_312a\_Lot2). This work is also supported through a contribution by the National Physical Laboratory, UK to the studentship. We  
thank NOAA ESRL and CU-INSTAAR for providing CH<sub>4</sub> and  $\delta^{13}\text{C}$  data. We thank the Japanese National Institute for Environmental  
555 Studies and the Ministry of Environment for the GOSAT data and their continuous support as part of the Joint Research Agreements at the  
Universities of Edinburgh and Leicester. We also thank the GEOS-Chem community, particularly the team at Harvard who help maintain the  
GEOS-Chem model, and the NASA Global Modeling and Assimilation Office (GMAO) who provide the MERRA-2 data product.

## References

- Allen, R. J., Zhao, X., Randles, C. A., Kramer, R. J., Samset, B. H., and Smith, C. J.: Surface warming and wetting due to methane's  
560 long-wave radiative effects muted by short-wave absorption, *Nature Geoscience*, 16, 314–320, 2023.
- Basu, S., Lan, X., Dlugokencky, E., Michel, S., Schwietzke, S., Miller, J. B., Bruhwiler, L., Oh, Y., Tans, P. P., Apadula, F., Gatti, L. V.,  
Jordan, A., Necki, J., Sasakawa, M., Morimoto, S., Di Iorio, T., Lee, H., Arduini, J., and Manca, G.: Estimating Emissions of Methane  
Consistent with Atmospheric Measurements of Methane and  $\delta^{13}\text{C}$  of Methane, *Atmospheric Chemistry and Physics Discussions*, 2022,  
1–38, <https://doi.org/10.5194/acp-2022-317>, 2022.
- 565 Bey, I., Jacob, D. J., Yantosca, R. M., Logan, J. A., Field, B. D., Fiore, A. M., Li, Q., Liu, H. Y., Mickley, L. J., and Schultz, M. G.: Global  
modeling of tropospheric chemistry with assimilated meteorology: Model description and evaluation, *Journal of Geophysical Research  
Atmospheres*, 106, 23 073–23 095, <https://doi.org/10.1029/2001JD000807>, 2001.
- Bloom, A. A., Bowman, K. W., Lee, M., Turner, A. J., Schroeder, R., Worden, J. R., Weidner, R., McDonald, K. C., and Jacob, D. J.: A global  
wetland methane emissions and uncertainty dataset for atmospheric chemical transport models (WetCHARTs version 1.0), *Geosci. Model  
570 Dev*, 10, 2141–2156, <https://doi.org/10.5194/gmd-10-2141-2017>, 2017.
- Burkholder, J. B., Sander, S. P., Abbatt, J., Barker, J. R., Cappa, C., Crouse, J. D., Dibble, T. S. and Huie, R. E., Kolb, C. E., Kurylo, M. J.,  
Orkin, V. L., Percival, C. J., Wilmouth, D. M., and Wine, P. H.: Chemical Kinetics and Photochemical Data for Use in Atmospheric  
Studies, Evaluation No. 19, Tech. rep., JPL Publication 19-5, Jet Propulsion Laboratory, Pasadena, 2019.
- Chung, E. and Arnold, T.: Potential of Clumped Isotopes in Constraining the Global Atmospheric Methane Budget, *Global Biogeochemical  
575 Cycles*, 35, e2020GB006 883, <https://doi.org/10.1029/2020GB006883>, e2020GB006883 2020GB006883, 2021.
- Cooper, M. J., Martin, R. V., Hammer, M. S., Levelt, P. F., Veefkind, P., Lamsal, L. N., Krotkov, N. A., Brook, J. R., and McLinden, C. A.:  
Global fine-scale changes in ambient NO<sub>2</sub> during COVID-19 lockdowns, *Nature*, 601, 380–387, 2022.
- Crippa, M., Guizzardi, D., Muntean, M., Schaaf, E., Lo Vullo, E., Solazzo, E., Monforti-Ferrario, F., Olivier, J., and Vignati, E.: EDGAR v6.0  
Greenhouse Gas Emissions, <http://data.europa.eu/89h/97a67d67-c62e-4826-b873-9d972c4f670b>, European Commission, Joint Research  
580 Centre (JRC) [Dataset], 2021.
- Dlugokencky, E., Crotwell, A., Mund, J., and Thoning, K.: Atmospheric Methane Dry Air Mole Fractions from the NOAA GML Carbon  
Cycle Cooperative Global Air Sampling Network, 1983–2019, Version: 2020-07, <https://doi.org/https://doi.org/10.15138/VNCZ-M766>,  
2020.
- Dlugokencky, E. J., Myers, R. C., Lang, P. M., Masarie, K. A., Crotwell, A. M., Thoning, K. W., Hall, B. D., Elkins, J. W., and Steele,  
585 L. P.: Conversion of NOAA atmospheric dry air CH<sub>4</sub> mole fractions to a gravimetrically prepared standard scale, *Journal of Geophysical  
Research: Atmospheres*, 110, <https://doi.org/10.1029/2005JD006035>, 2005.
- Dlugokencky, E., Steele, L., Lang, P., and Masarie, K.: The growth rate and distribution of atmospheric methane, *Journal of Geophysical  
Research: Atmospheres*, 99, 17 021–17 043, <https://doi.org/https://doi.org/10.1029/94JD01245>, 1994.
- Douglas, P. M., Stolper, D. A., Eiler, J. M., Sessions, A. L., Lawson, M., Shuai, Y., Bishop, A., Podlaha, O. G., Ferreira, A. A., Santos Neto,  
590 E. V., Niemann, M., Steen, A. S., Huang, L., Chimiak, L., Valentine, D. L., Fiebig, J., Luhmann, A. J., Seyfried, W. E., Etiopie, G., Schoell,  
M., Inskeep, W. P., Moran, J. J., and Kitchen, N.: Methane clumped isotopes: Progress and potential for a new isotopic tracer, *Organic  
Geochemistry*, 113, 262–282, <https://doi.org/10.1016/j.orggeochem.2017.07.016>, 2017.
- Duncan, B. N., Strahan, S. E., Yoshida, Y., Steenrod, S. D., and Livesey, N.: Model study of the cross-tropopause transport of biomass  
burning pollution, *Atmospheric Chemistry and Physics*, 7, 3713–3736, <https://doi.org/10.5194/acp-7-3713-2007>, 2007.

- 595 Feilberg, K. L., Griffith, D. W. T., Johnson, M. S., and Nielsen, C. J.: The  $^{13}\text{C}$  and D kinetic isotope effects in the reaction of  $\text{CH}_4$  with Cl, *International Journal of Chemical Kinetics*, 37, 110–118, <https://doi.org/https://doi.org/10.1002/kin.20058>, 2005.
- Feng, L., Palmer, P. I., Bösch, H., Parker, R. J., Webb, A. J., Correia, C. S. C., Deutscher, N. M., Domingues, L. G., Feist, D. G., Gatti, L. V., Gloor, E., Hase, F., Kivi, R., Liu, Y., Miller, J. B., Morino, I., Sussmann, R., Strong, K., Uchino, O., Wang, J., and Zahn, A.: Consistent regional fluxes of  $\text{CH}_4$  and  $\text{CO}_2$  inferred from GOSAT proxy  $\text{XCH}_4$ :  $\text{XCO}_2$  retrievals, 2010–2014, *Atmospheric Chemistry and Physics*, 600 17, 4781–4797, <https://doi.org/10.5194/acp-17-4781-2017>, 2017.
- Feng, L., Palmer, P. I., Zhu, S., Parker, R. J., and Liu, Y.: Tropical methane emissions explain large fraction of recent changes in global atmospheric methane growth rate, *Nature Communications*, 13, 1378, <https://doi.org/10.1038/s41467-022-28989-z>, 2022.
- Feng, L., Palmer, P. I., Parker, R. J., Lunt, M. F., and Bösch, H.: Methane emissions are predominantly responsible for record-breaking atmospheric methane growth rates in 2020 and 2021, *Atmospheric Chemistry and Physics*, 23, 4863–4880, <https://doi.org/10.5194/acp-23-4863-2023>, 2023.
- Fraser, A., Palmer, P. I., Feng, L., Bösch, H., Parker, R., Dlugokencky, E. J., Krummel, P. B., and Langenfelds, R. L.: Estimating regional fluxes of  $\text{CO}_2$  and  $\text{CH}_4$  using space-borne observations of  $\text{XCH}_2$ :  $\text{XCO}_2$ , *Atmospheric Chemistry and Physics*, 14, 12883–12895, <https://doi.org/10.5194/acp-14-12883-2014>, 2014.
- Fujita, R., Morimoto, S., Maksyutov, S., Kim, H.-S., Arshinov, M., Brailsford, G., Aoki, S., and Nakazawa, T.: Global and Regional  $\text{CH}_4$  Emissions for 1995–2013 Derived From Atmospheric  $\text{CH}_4$ ,  $\delta^{13}\text{C}-\text{CH}_4$ , and  $\delta\text{D}-\text{CH}_4$  Observations and a Chemical Transport Model, *Journal of Geophysical Research: Atmospheres*, 125, e2020JD032903, <https://doi.org/https://doi.org/10.1029/2020JD032903>, e2020JD032903 2020JD032903, 2020.
- Fung, I., John, J., Lerner, J., Matfhevs, E., Prather, M., Steele, L. P., and Fraser, P. J.: <Three-dimensional model synthesis of the global methane cycle-Fung 1991.pdf>, *JOURNAL OF GEOPHYSICAL RESEARCH*, 96, 33–46, [https://pubs.giss.nasa.gov/docs/1991/1991\\_{\\_}Fung\\_{\\_}fu08000d.pdf](https://pubs.giss.nasa.gov/docs/1991/1991_{_}Fung_{_}fu08000d.pdf), 1991.
- 615 Ganesan, A. L., Stell, A. C., Gedney, N., Comyn-Platt, E., Hayman, G., Rigby, M., Poulter, B., and Hornibrook, E. R. C.: Spatially Resolved Isotopic Source Signatures of Wetland Methane Emissions, *Geophysical Research Letters*, 45, 3737–3745, <https://doi.org/10.1002/2018GL077536>, 2018.
- Gelaro, R., McCarty, W., Suárez, M. J., Todling, R., Molod, A., Takacs, L., Randles, C. A., Darmenov, A., Bosilovich, M. G., Reichle, R., 620 Wargan, K., Coy, L., Cullather, R., Draper, C., Akella, S., Buchard, V., Conaty, A., da Silva, A. M., Gu, W., Kim, G. K., Koster, R., Lucchesi, R., Merkova, D., Nielsen, J. E., Partyka, G., Pawson, S., Putman, W., Rienecker, M., Schubert, S. D., Sienkiewicz, M., and Zhao, B.: The modern-era retrospective analysis for research and applications, version 2 (MERRA-2), *Journal of Climate*, 30, 5419–5454, <https://doi.org/10.1175/JCLI-D-16-0758.1>, 2017.
- Gurney, K. R., Law, R. M., Denning, A. S., Rayner, P. J., Baker, D., Bousquet, P., Bruhwiler, L., Chen, Y.-H., Ciais, P., Fan, S., Fung, I. Y., 625 Gloor, M., Heimann, M., Higuchi, K., John, J., Maki, T., Maksyutov, S., Masarie, K., Peylin, P., Prather, M., Pak, B. C., Randerson, J., Sarmiento, J., Taguchi, S., Takahashi, T., and Yuen, C.-W.: Towards robust regional estimates of  $\text{CO}_2$  sources and sinks using atmospheric transport models, *Nature*, 415, 626–630, <https://doi.org/10.1038/415626a>, 2002.
- Janssens-Maenhout, G., Crippa, M., Guizzardi, D., Muntean, M., Schaaf, E., Dentener, F., Bergamaschi, P., Pagliari, V., Olivier, J. G. J., Peters, J. A. H. W., van Aardenne, J. A., Monni, S., Doering, U., Petrescu, A. M. R., Solazzo, E., and Oreggioni, G. D.: EDGAR v4.3.2 Global Atlas of the three major greenhouse gas emissions for the period 1970–2012, *Earth System Science Data*, 11, 959–1002, 630 <https://doi.org/10.5194/essd-11-959-2019>, 2019.

- Kirschke, S., Bousquet, P., Ciais, P., Saunoy, M., Canadell, J. G., Dlugokencky, E. J., Bergamaschi, P., Bergmann, D., Blake, D. R., Bruhwiler, L., Cameron-Smith, P., Castaldi, S., Chevallier, F., Feng, L., Fraser, A., Heimann, M., Hodson, E. L., Houweling, S., Josse, B., Fraser, P. J., Krummel, P. B., Lamarque, J. F., Langenfelds, R. L., Le Quére, C., Naik, V., O'doherty, S., Palmer, P. I., Pison, I., Plummer, D., Poulter, B., Prinn, R. G., Rigby, M., Ringeval, B., Santini, M., Schmidt, M., Shindell, D. T., Simpson, I. J., Spahni, R., Steele, L. P., Strode, S. A., Sudo, K., Szopa, S., Van Der Werf, G. R., Voulgarakis, A., Van Weele, M., Weiss, R. F., Williams, J. E., and Zeng, G.: Three decades of global methane sources and sinks, <https://doi.org/10.1038/ngeo1955>, 2013.
- Lan, X., Basu, S., Schwietzke, S., Bruhwiler, L. M. P., Dlugokencky, E. J., Michel, S. E., Sherwood, O. A., Tans, P. P., Thoning, K., Etiope, G., Zhuang, Q., Liu, L., Oh, Y., Miller, J. B., Pétron, G., Vaughn, B. H., and Crippa, M.: Improved Constraints on Global Methane Emissions and Sinks Using  $\delta^{13}\text{C}\text{-CH}_4$ , *Global Biogeochemical Cycles*, 35, e2021GB007000, <https://doi.org/https://doi.org/10.1029/2021GB007000>, e2021GB007000 2021GB007000, 2021.
- Laughner, J. L., Neu, J. L., Schimel, D., Wennberg, P. O., Barsanti, K., Bowman, K. W., Chatterjee, A., Croes, B. E., Fitzmaurice, H. L., Henze, D. K., Kim, J., Kort, E. A., Liu, Z., Miyazaki, K., Turner, A. J., Anenberg, S., Avise, J., Cao, H., Crisp, D., de Gouw, J., Eldering, A., Fyfe, J. C., Goldberg, D. L., Gurney, K. R., Hasheminassab, S., Hopkins, F., Ivey, C. E., Jones, D. B. A., Liu, J., Lovenduski, N. S., Martin, R. V., McKinley, G. A., Ott, L., Poulter, B., Ru, M., Sander, S. P., Swart, N., Yung, Y. L., and Zeng, Z.-C.: Societal shifts due to COVID-19 reveal large-scale complexities and feedbacks between atmospheric chemistry and climate change, *Proceedings of the National Academy of Sciences*, 118, <https://doi.org/10.1073/pnas.2109481118>, 2021.
- Lunt, M. F., Palmer, P. I., Feng, L., Taylor, C. M., Boesch, H., and Parker, R. J.: An increase in methane emissions from tropical Africa between 2010 and 2016 inferred from satellite data, *Atmospheric Chemistry and Physics*, 19, 14 721–14 740, <https://doi.org/10.5194/acp-19-14721-2019>, 2019.
- Lunt, M. F., Palmer, P. I., Lorente, A., Borsdorff, T., Landgraf, J., Parker, R. J., and Boesch, H.: Rain-fed pulses of methane from East Africa during 2018–2019 contributed to atmospheric growth rate, *Environmental Research Letters*, 16, 024 021, <https://doi.org/10.1088/1748-9326/abd8fa>, 2021.
- Masson-Delmotte, V., Zhai, P., A. Pirani, S. C., C. Péan, S. B., Caud, N., Chen, Y., Gomis, L. G. M., Huang, M., Leitzell, K., Lonnoy, E., Matthews, J., Maycock, T., Waterfield, T., Yelekçi, O., Yu, R., and Zhou, B.: Climate Change 2021: The Physical Science Basis. Contribution of Working Group I to the Sixth Assessment Report of the Intergovernmental Panel on Climate Changes, Tech. rep., IPCC, WMO Geneva, 2021.
- McNorton, J., Chipperfield, M. P., Gloor, M., Wilson, C., Feng, W., Hayman, G. D., Rigby, M., Krummel, P. B., O'Doherty, S., Prinn, R. G., Weiss, R. F., Young, D., Dlugokencky, E., and Montzka, S. A.: Role of OH variability in the stalling of the global atmospheric  $\text{CH}_4$  growth rate from 1999 to 2006, *Atmospheric Chemistry and Physics*, 16, 7943–7956, <https://doi.org/10.5194/acp-16-7943-2016>, 2016.
- McNorton, J., Wilson, C., Gloor, M., Parker, R., Boesch, H., Feng, W., and Chipperfield, M.: Attribution of recent increases in atmospheric methane through 3-D inverse modelling, *Atmos. Chem. Phys.*, 18, 1–34, <https://doi.org/10.5194/acp-2018-474>, 2018.
- Miller, J. B.: Development of analytical methods and measurements of  $^{13}\text{C}/^{12}\text{C}$  in atmospheric  $\text{CH}_4$  from the NOAA Climate Monitoring and Diagnostics Laboratory Global Air Sampling Network, *Journal of Geophysical Research*, 107, 4178, <https://doi.org/10.1029/2001JD000630>, 2002.
- Miyazaki, K., Bowman, K., Sekiya, T., Takigawa, M., Neu, J. L., Sudo, K., Osterman, G., and Eskes, H.: Global tropospheric ozone responses to reduced  $\text{NO}_x$  emissions linked to the COVID-19 worldwide lockdowns, *Science Advances*, 7, eabf7460, <https://doi.org/10.1126/sciadv.abf7460>, 2021.

- Morgenstern, O., Hegglin, M. I., Rozanov, E., O'Connor, F. M., Abraham, N. L., Akiyoshi, H., Archibald, A. T., Bekki, S., Butchart, N.,  
670 Chipperfield, M. P., Deushi, M., Dhomse, S. S., Garcia, R. R., Hardiman, S. C., Horowitz, L. W., Jöckel, P., Josse, B., Kinnison, D.,  
Lin, M., Mancini, E., Manyin, M. E., Marchand, M., Marécal, V., Michou, M., Oman, L. D., Pitari, G., Plummer, D. A., Revell, L. E.,  
Saint-Martin, D., Schofield, R., Stenke, A., Stone, K., Sudo, K., Tanaka, T. Y., Tilmes, S., Yamashita, Y., Yoshida, K., and Zeng, G.:  
Review of the global models used within phase 1 of the Chemistry–Climate Model Initiative (CCMI), *Geoscientific Model Development*,  
10, 639–671, <https://doi.org/10.5194/gmd-10-639-2017>, 2017.
- 675 Nisbet, E. G., Dlugokencky, E. J., Manning, M. R., Lowry, D., Fisher, R. E., France, J. L., Michel, S. E., Miller, J. B., White, J. W., Vaughn,  
B., Bousquet, P., Pyle, J. A., Warwick, N. J., Cain, M., Brownlow, R., Zazzeri, G., Lanoisellé, M., Manning, A. C., Gloor, E., Worthy,  
D. E., Brunke, E. G., Labuschagne, C., Wolff, E. W., and Ganesan, A. L.: Rising atmospheric methane: 2007–2014 growth and isotopic  
shift, *Global Biogeochemical Cycles*, 30, 1356–1370, <https://doi.org/10.1002/2016GB005406>, 2016.
- Nisbet, E. G., Manning, M. R., Dlugokencky, E. J., Fisher, R. E., Lowry, D., Michel, S. E., Myhre, C. L., Platt, S. M., Allen, G., Bousquet,  
680 P., Brownlow, R., Cain, M., France, J. L., Hermansen, O., Hossaini, R., Jones, A. E., Levin, I., Manning, A. C., Myhre, G., Pyle, J. A.,  
Vaughn, B. H., Warwick, N. J., and White, J. W. C.: Very Strong Atmospheric Methane Growth in the 4 Years 2014–2017: Implications  
for the Paris Agreement, *Global Biogeochemical Cycles*, 33, 318–342, <https://doi.org/https://doi.org/10.1029/2018GB006009>, 2019.
- Palmer, P. I., Feng, L., Lunt, M. F., Parker, R. J., Bösch, H., Lan, X., Lorente, A., and Borsdorff, T.: The added value of satellite observations of  
methane for understanding the contemporary methane budget, *Philosophical Transactions of the Royal Society A: Mathematical, Physical*  
685 *and Engineering Sciences*, 379, 20210 106, <https://doi.org/10.1098/rsta.2021.0106>, 2021.
- Pandey, S., Houweling, S., Lorente, A., Borsdorff, T., Tsvilidou, M., Bloom, A. A., Poulter, B., Zhang, Z., and Aben, I.: Using satellite data to  
identify the methane emission controls of South Sudan's wetlands, *Biogeosciences*, 18, 557–572, <https://doi.org/10.5194/bg-18-557-2021>,  
2021.
- Parker, R., Boesch, H., Cogan, A., Fraser, A., Feng, L., Palmer, P. I., Messerschmidt, J., Deutscher, N., Griffith, D. W. T., Notholt, J.,  
690 Wennberg, P. O., and Wunch, D.: Methane observations from the Greenhouse Gases Observing SATellite: Comparison to ground-based  
TCCON data and model calculations, *Geophysical Research Letters*, 38, <https://doi.org/https://doi.org/10.1029/2011GL047871>, 2011.
- Parker, R. J., Boesch, H., Byckling, K., Webb, A. J., Palmer, P. I., Feng, L., Bergamaschi, P., Chevallier, F., Notholt, J., Deutscher, N.,  
Warneke, T., Hase, F., Sussmann, R., Kawakami, S., Kivi, R., Griffith, D. W. T., and Velazco, V.: Assessing 5 years of GOSAT Proxy  
XCH<sub>4</sub> data and associated uncertainties, *Atmospheric Measurement Techniques*, 8, 4785–4801, <https://doi.org/10.5194/amt-8-4785-2015>,  
695 2015.
- Parker, R. J., Webb, A., Boesch, H., Somkuti, P., Barrio Guillo, R., Di Noia, A., Kalaitzi, N., Anand, J. S., Bergamaschi, P., Chevallier,  
F., Palmer, P. I., Feng, L., Deutscher, N. M., Feist, D. G., Griffith, D. W. T., Hase, F., Kivi, R., Morino, I., Notholt, J., Oh, Y.-S.,  
Ohyama, H., Petri, C., Pollard, D. F., Roehl, C., Sha, M. K., Shiomi, K., Strong, K., Sussmann, R., Té, Y., Velazco, V. A., Warneke,  
T., Wennberg, P. O., and Wunch, D.: A decade of GOSAT Proxy satellite CH<sub>4</sub> observations, *Earth System Science Data*, 12, 3383–3412,  
700 <https://doi.org/10.5194/essd-12-3383-2020>, 2020.
- Peng, S., Lin, X., Thompson, R. L., Xi, Y., Liu, G., Hauglustaine, D., Lan, X., Poulter, B., Ramonet, M., Saunio, M., Yin, Y., Zhang, Z.,  
Zheng, B., and Ciais, P.: Wetland emission and atmospheric sink changes explain methane growth in 2020, *Nature*, 612, 477–482, 2022.
- Qu, Z., Jacob, D. J., Zhang, Y., Shen, L., Varon, D. J., Lu, X., Scarpelli, T., Bloom, A., Worden, J., and Parker, R. J.: Attribution of  
the 2020 surge in atmospheric methane by inverse analysis of GOSAT observations, *Environmental Research Letters*, 17, 094 003,  
705 <https://doi.org/10.1088/1748-9326/ac8754>, 2022.

- Randerson, J., Van Der Werf, G., Giglio, L., Collatz, G., and Kasibhatla, P.: Global Fire Emissions Database, Version 4.1 (GFEDv4), <https://doi.org/10.3334/ORNLDAAC/1293>, 2017.
- Rice, A. L., Butenhoff, C. L., Teama, D. G., Röger, F. H., Khalil, M. A. K., and Rasmussen, R. A.: Atmospheric methane isotopic record favors fossil sources flat in 1980s and 1990s with recent increase, *Proceedings of the National Academy of Sciences*, 113, 10791–10796, <https://doi.org/10.1073/pnas.1522923113>, 2016.
- 710 Rigby, M., Montzka, S. A., Prinn, R. G., White, J. W. C., Young, D., O'Doherty, S., Lunt, M. F., Ganesan, A. L., Manning, A. J., Simmonds, P. G., Salameh, P. K., Harth, C. M., Mühle, J., Weiss, R. F., Fraser, P. J., Steele, L. P., Krümmel, P. B., McCulloch, A., and Park, S.: Role of atmospheric oxidation in recent methane growth, *Proceedings of the National Academy of Sciences*, 114, 5373–5377, <https://doi.org/10.1073/pnas.1616426114>, 2017.
- 715 Rodgers, C. D. C. D.: *Inverse methods for atmospheric sounding : theory and practice*, Series on atmospheric, oceanic and planetary physics ; vol. 2, World Scientific, Singapore ; London, 2000.
- Sasakawa, M., Shimoyama, K., Machida, T., Tsuda, N., Suto, H., Arshinov, M., Davydov, D., Fofonov, A., Krasnov, O., Saeki, T., Koyama, Y., and Maksyutov, S.: Continuous measurements of methane from a tower network over Siberia, *Tellus B*, 62, 403–416, <https://doi.org/https://doi.org/10.1111/j.1600-0889.2010.00494.x>, 2010.
- 720 Saunio, M., Stavert, A. R., Poulter, B., Bousquet, P., Canadell, J. G., Jackson, R. B., Raymond, P. A., Dlugokencky, E. J., Houweling, S., Patra, P. K., Ciais, P., Arora, V. K., Bastviken, D., Bergamaschi, P., Blake, D. R., Brailsford, G., Bruhwiler, L., Carlson, K. M., Carrol, M., Castaldi, S., Chandra, N., Crevoisier, C., Crill, P. M., Covey, K., Curry, C. L., Etiope, G., Frankenberg, C., Gedney, N., Hegglin, M. I., Höglund-Isaksson, L., Hugelius, G., Ishizawa, M., Ito, A., Janssens-Maenhout, G., Jensen, K. M., Joos, F., Kleinen, T., Krümmel, P. B., Langenfelds, R. L., Laruelle, G. G., Liu, L., Machida, T., Maksyutov, S., McDonald, K. C., McNorton, J., Miller, P. A., Melton,
- 725 J. R., Morino, I., Müller, J., Murguía-Flores, F., Naik, V., Niwa, Y., Noce, S., O'Doherty, S., Parker, R. J., Peng, C., Peng, S., Peters, G. P., Prigent, C., Prinn, R., Ramonet, M., Regnier, P., Riley, W. J., Rosentretter, J. A., Segers, A., Simpson, I. J., Shi, H., Smith, S. J., Steele, L. P., Thornton, B. F., Tian, H., Tohjima, Y., Tubiello, F. N., Tsuruta, A., Viovy, N., Voulgarakis, A., Weber, T. S., van Weele, M., van der Werf, G. R., Weiss, R. F., Worthy, D., Wunch, D., Yin, Y., Yoshida, Y., Zhang, W., Zhang, Z., Zhao, Y., Zheng, B., Zhu, Q., Zhu, Q., and Zhuang, Q.: The Global Methane Budget 2000–2017, *Earth System Science Data*, 12, 1561–1623, <https://doi.org/10.5194/essd-12-1561-2020>,
- 730 2020.
- Schaefer, H., Schaefer, H., Fletcher, S. E. M., Veidt, C., Lassey, K. R., Brailsford, G. W., Bromley, M., Dlugokencky, E. J., Michel, S. E., Miller, J. B., Levin, I., Lowe, D. C., Martin, J., Vaughn, B. H., and White, J. W. C.: A 21st century shift from fossil-fuel to biogenic methane emissions indicated by  $^{13}\text{CH}_4$ , *Science*, 2705, 1–10, 2016.
- Schuldt, K. N., Aalto, T., Andrews, A., Aoki, S., Arduini, J., Baier, B., Bergamaschi, P., Biermann, T., Biraud, S. C., Boenisch, H., Brailsford,
- 735 G., Chen, H., Colomb, A., Conil, S., Cristofanelli, P., Cuevas, E., Daube, B., Davis, K., Mazière, M. D., Delmotte, M., Desai, A., DiGangi, J. P., Dlugokencky, E., Elkins, J. W., Emmenegger, L., Fischer, M. L., Gatti, L. V., Gehrlein, T., Gerbig, C., Gloor, E., Goto, D., Haszpra, L., Hatakka, J., Heimann, M., Heliasz, M., Hermanssen, O., Hintsä, E., Holst, J., Ivakhov, V., Jaffe, D., Joubert, W., Kang, H.-Y., Karion, A., Kazan, V., Keronen, P., Ko, M.-Y., Kominkova, K., Kort, E., Kozlova, E., Krümmel, P., Kubistin, D., Labuschagne, C., Langenfelds, R., Laurent, O., Laurila, T., Lauvaux, T., Lee, J., Lee, H., Lee, C.-H., Lehner, I., Leppert, R., Leuenberger, M., Lindauer, M., Loh, Z.,
- 740 Lopez, M., Machida, T., Mammarella, I., Manca, G., Marek, M. V., Martin, M. Y., Matsueda, H., McKain, K., Miles, N., Miller, C. E., Miller, J. B., Moore, F., Morimoto, S., Munro, D., Myhre, C. L., Mölder, M., Müller-Williams, J., Nichol, S., Niwa, Y., O'Doherty, S., Obersteiner, F., Piacentino, S., Pichon, J. M., Pittman, J., Plass-Duelmer, C., Ramonet, M., Richardson, S., Rivas, P. P., Saito, K., Santoni, G., Sasakawa, M., Scheeren, B., Schuck, T., Schumacher, M., Seifert, T., Sha, M. K., Shepson, P., Sloop, C. D., Smith, P., Steinbacher,

- M., Stephens, B., Sweeney, C., Timas, H., Torn, M., Trisolino, P., Turnbull, J., Tørseth, K., Viner, B., Vitkova, G., Watson, A., Wofsy, S.,  
745 Worsley, J., Worthy, D., Zahn, A., and di Sarra, A. G.: Multi-laboratory compilation of atmospheric methane data for the period 1983-2020;  
obspack\_ch4\_1\_GLOBALVIEWplus\_v4.0\_2021-10-14, <https://doi.org/http://doi.org/10.25925/20211001>, 2021.
- Sheng, J., Tunnicliffe, R., Ganesan, A. L., Maasackers, J. D., Shen, L., Prinn, R. G., Song, S., Zhang, Y., Scarpelli, T., Bloom, A. A.,  
Rigby, M., Manning, A. J., Parker, R. J., Boesch, H., Lan, X., Zhang, B., Zhuang, M., and Lu, X.: Sustained methane emis-  
sions from China after 2012 despite declining coal production and rice-cultivated area, *Environmental Research Letters*, 16, 104018,  
750 <https://doi.org/10.1088/1748-9326/ac24d1>, 2021.
- Sherwen, T., Schmidt, J. A., Evans, M. J., Carpenter, L. J., Großmann, K., Eastham, S. D., Jacob, D. J., Dix, B., Koenig, T. K., Sinreich, R., Or-  
tega, I., Volkamer, R., Saiz-Lopez, A., Prados-Roman, C., Mahajan, A. S., and Ordóñez, C.: Global impacts of tropospheric halogens (Cl,  
Br, I) on oxidants and composition in GEOS-Chem, *Atmospheric Chemistry and Physics*, 16, 12 239–12 271, <https://doi.org/10.5194/acp-16-12239-2016>, 2016.
- 755 Sherwood, O. A., Schwietzke, S., Arling, V. A., and Etiope, G.: Global inventory of gas geochemistry data from fossil fuel, microbial and  
burning sources, version 2017, *Earth System Science Data*, 9, 639–656, <https://doi.org/10.5194/essd-9-639-2017>, 2017.
- Siegel, A. F.: Robust regression using repeated medians, Tech. rep., Princeton University, 1980.
- Snover, A. K. and Quay, P. D.: Hydrogen and carbon kinetic isotope effects during soil uptake of atmospheric methane, *Global Biogeochem-  
ical Cycles*, 14, 25–39, <https://doi.org/10.1029/1999GB900089>, 2000.
- 760 Steele, L. P., Fraser, P. J., Rasmussen, R. A., Khalil, M. A. K., Conway, T. J., Crawford, A. J., Gammon, R. H., Masarie, K. A., and Thoning,  
K. W.: The Global Distribution of Methane in the Troposphere, pp. 417–463, Springer Netherlands, 1987.
- Turner, A. J., Frankenberg, C., Wennberg, P. O., and Jacob, D. J.: Ambiguity in the causes for decadal trends in atmospheric methane and  
hydroxyl, *Proceedings of the National Academy of Sciences*, 114, 5367–5372, <https://doi.org/10.1073/pnas.1616020114>, 2017.
- Turner, A. J., Frankenberg, C., and Kort, E. A.: Interpreting contemporary trends in atmospheric methane, *Proceedings of the National  
765 Academy of Sciences*, 116, 201814 297, <https://doi.org/10.1073/pnas.1814297116>, 2019.
- Vaughn, B., Miller, J., Ferretti, D., and White, J.: Stable isotope measurements of atmospheric CO<sub>2</sub> and CH<sub>4</sub>, *Handbook of Stable Isotope  
Analytical Techniques*, vol 1, chap. 14, Elsevier, 2004.
- Voulgarakis, A., Naik, V., Lamarque, J.-F., Shindell, D. T., Young, P. J., Prather, M. J., Wild, O., Field, R. D., Bergmann, D., Cameron-  
Smith, P., Cionni, I., Collins, W. J., Dalsøren, S. B., Doherty, R. M., Eyring, V., Faluvegi, G., Folberth, G. A., Horowitz, L. W., Josse, B.,  
770 McKenzie, I. A., Nagashima, T., Plummer, D. A., Righi, M., Rumbold, S. T., Stevenson, D. S., Strode, S. A., Sudo, K., Szopa, S., and  
Zeng, G.: Analysis of present day and future OH and methane lifetime in the ACCMIP simulations, *Atmos. Chem. Phys.*, 13, 2563–2587,  
<https://doi.org/10.5194/acp-13-2563-2013>, 2013.
- Wilson, C., Chipperfield, M. P., Gloor, M., Parker, R. J., Boesch, H., McNorton, J., Gatti, L. V., Miller, J. B., Basso, L. S., and Monks,  
S. A.: Large and increasing methane emissions from eastern Amazonia derived from satellite data, 2010–2018, *Atmospheric Chemistry  
775 and Physics*, 21, 10 643–10 669, <https://doi.org/10.5194/acp-21-10643-2021>, 2021.
- Worden, J., Bloom, A., Pandey, S., Jiang, Z., Worden, H., Walker, T., Houweling, S., and Röckmann, T.: Reduced biomass burning emissions  
reconcile conflicting estimates of the post-2006 atmospheric methane budget, *Nature Communications*, 8, <https://doi.org/10.1038/s41467-017-02246-0>, 2017.
- Yin, Y., Chevallier, F., Ciais, P., Bousquet, P., Saunoy, M., Zheng, B., Worden, J., Bloom, A. A., Parker, R. J., Jacob, D. J., Dlugokencky,  
780 E. J., and Frankenberg, C.: Accelerating methane growth rate from 2010 to 2017: leading contributions from the tropics and East Asia,  
*Atmospheric Chemistry and Physics*, 21, 12 631–12 647, <https://doi.org/10.5194/acp-21-12631-2021>, 2021.



- 785 Zhao, Y., Saunois, M., Bousquet, P., Lin, X., Berchet, A., Hegglin, M. I., Canadell, J. G., Jackson, R. B., Hauglustaine, D. A., Szopa, S., Stavert, A. R., Abraham, N. L., Archibald, A. T., Bekki, S., Deushi, M., Jöckel, P., Josse, B., Kinnison, D., Kirner, O., Marécal, V., O'Connor, F. M., Plummer, D. A., Revell, L. E., Rozanov, E., Stenke, A., Strode, S., Tilmes, S., Dlugokencky, E. J., and Zheng, B.: Inter-model comparison of global hydroxyl radical (OH) distributions and their impact on atmospheric methane over the 2000–2016 period, *Atmospheric Chemistry and Physics*, 19, 13 701–13 723, <https://doi.org/10.5194/acp-19-13701-2019>, 2019.
- Zhou, L., Kitzis, D., and Tans, P.: Report of the Fourth WMO Round-Robin Reference Gas Intercomparison, 2002-2007, Tech. rep., World Meteorological Organisation, 2009.

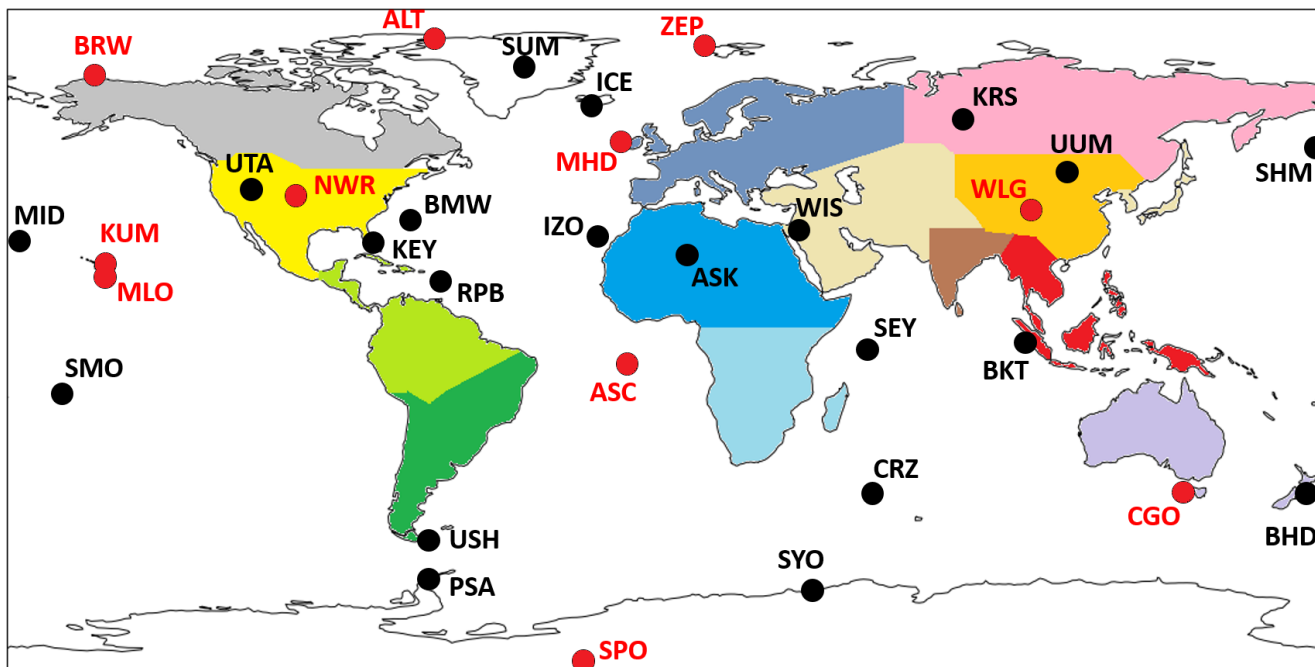


**Figure 1.** Map showing regions that are optimised in the CH<sub>4</sub> and δ<sup>13</sup>C inversions, in different colours. Black dots and labels show the location of ground-based measurement sites that measure CH<sub>4</sub> mole fraction. Red dots and labels indicate both mole fraction CH<sub>4</sub> and δ<sup>13</sup>C measuring sites. Regions are named as follows: Grey - North American Boreal; Yellow - North American Temperate; Light Green - South American Tropical; Dark Green - South American Temperate; Purple - Europe; Blue - North Africa; Light Blue - Southern Africa; Pink - Boreal Eurasia; Orange - China; Brown - India; Peach - Temperate Eurasia; Red - Tropical SE Asia; Lilac - Oceania; White - Oceans. Site identifiers are detailed in Table A2.

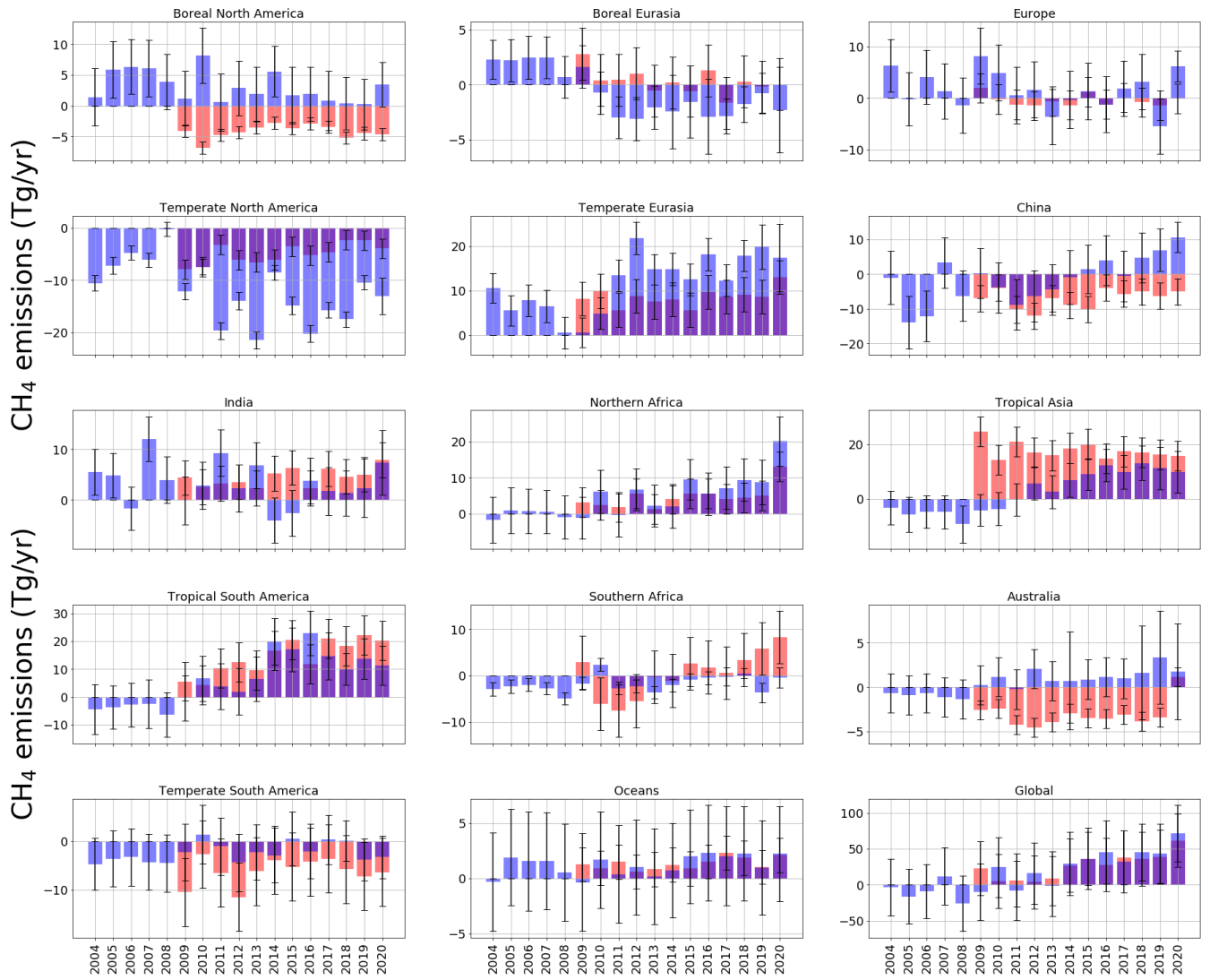


**Figure 2.** Annual mean CH<sub>4</sub> *a posteriori* emissions estimates as a residual value relative to *a priori* (Tg/yr) from each of the inversion regions in latitudinal order (geographic coverage indicated by Figure 1), for both ground-based and GOSAT inversion results. Uncertainties are indicated, as calculated from inversion calculations, with a *a priori* uncertainty of 50% for the ground-based results and 60% for the GOSAT results. The ground-based *a posteriori* is in blue; the GOSAT *a posteriori* are in red.

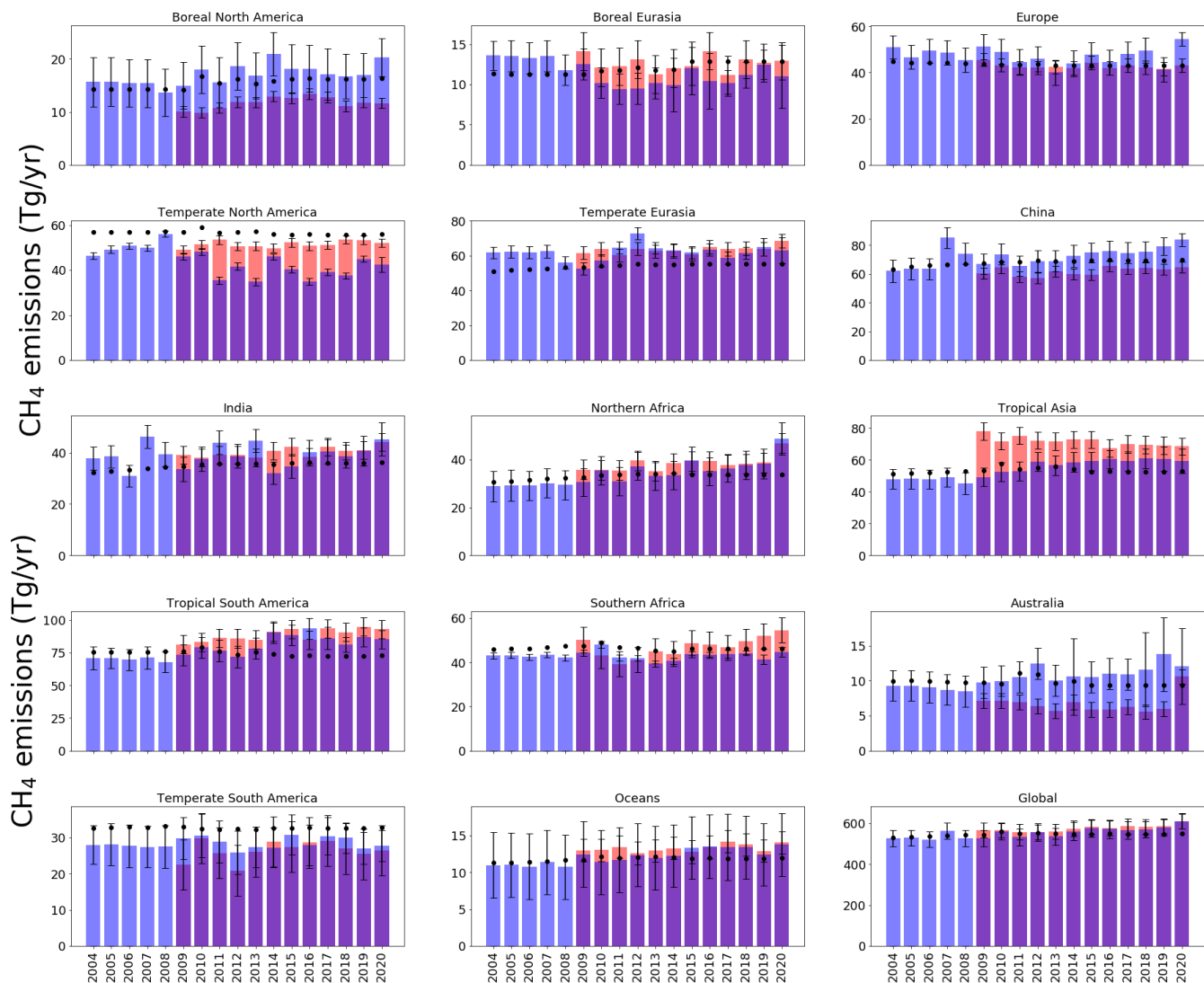


**Figure 3.** *A posteriori* emissions estimates (Tg/yr) inferred from ground-based *in situ* data (blue) and GOSAT data (red, with record starting in 2010) for the geographical regions shown by Figure 1. *A priori* emissions estimates are denoted by black dots and *a posteriori* uncertainties are denoted by whisker bars.

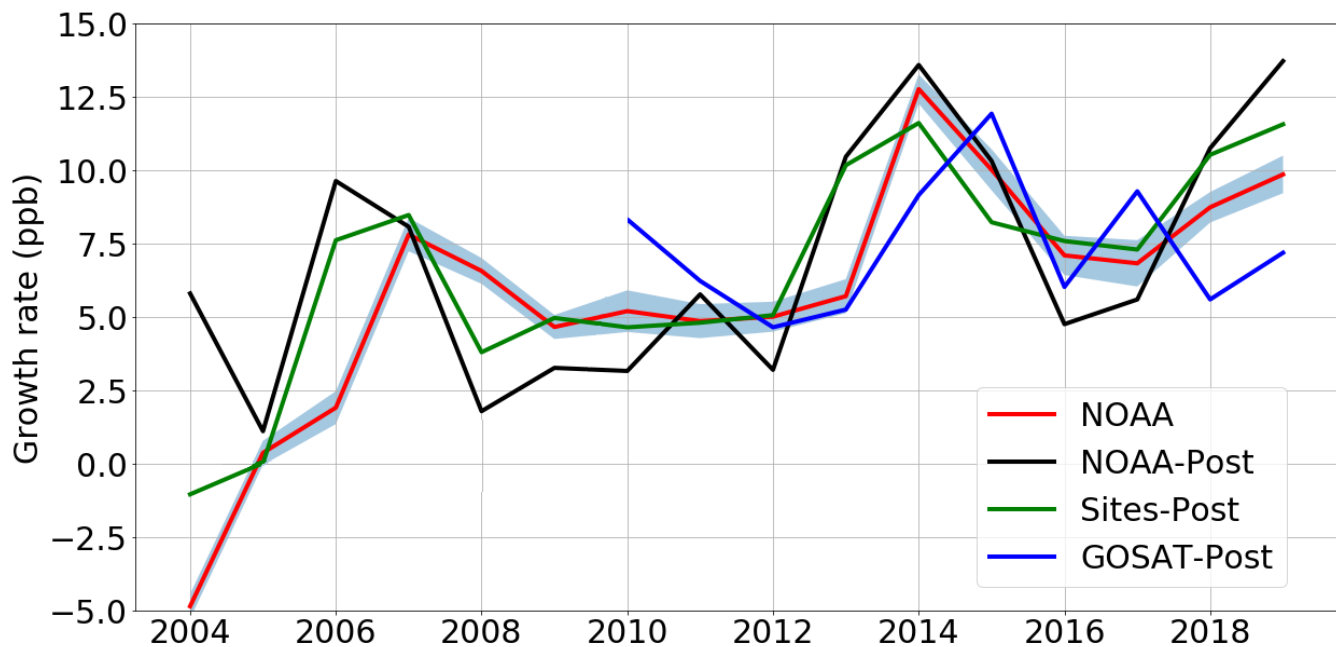


**Figure 4.** *A posteriori* annual mean atmospheric CH<sub>4</sub> growth rate inferred from *in situ* (black line) and GOSAT data (blue line) compared with the equivalent data as published by NOAA (red line, with uncertainty as blue surrounding field, Dlugokencky et al., 2020). The green line denotes the annual atmospheric growth rate determined using the *in situ* mole fraction data from the sites included in the inversion ('Sites-Post'). To calculate the atmospheric growth rates from model calculations (Ground-Post and GOSAT-post), we compare the average global CH<sub>4</sub> mole fraction in one year (the mean mole fraction of every grid box in every month of a year), with the mean value from the following year. The calculation is January-January, in order to remove the effects of the seasonal cycle, following the approach by NOAA (Dlugokencky et al., 2020).

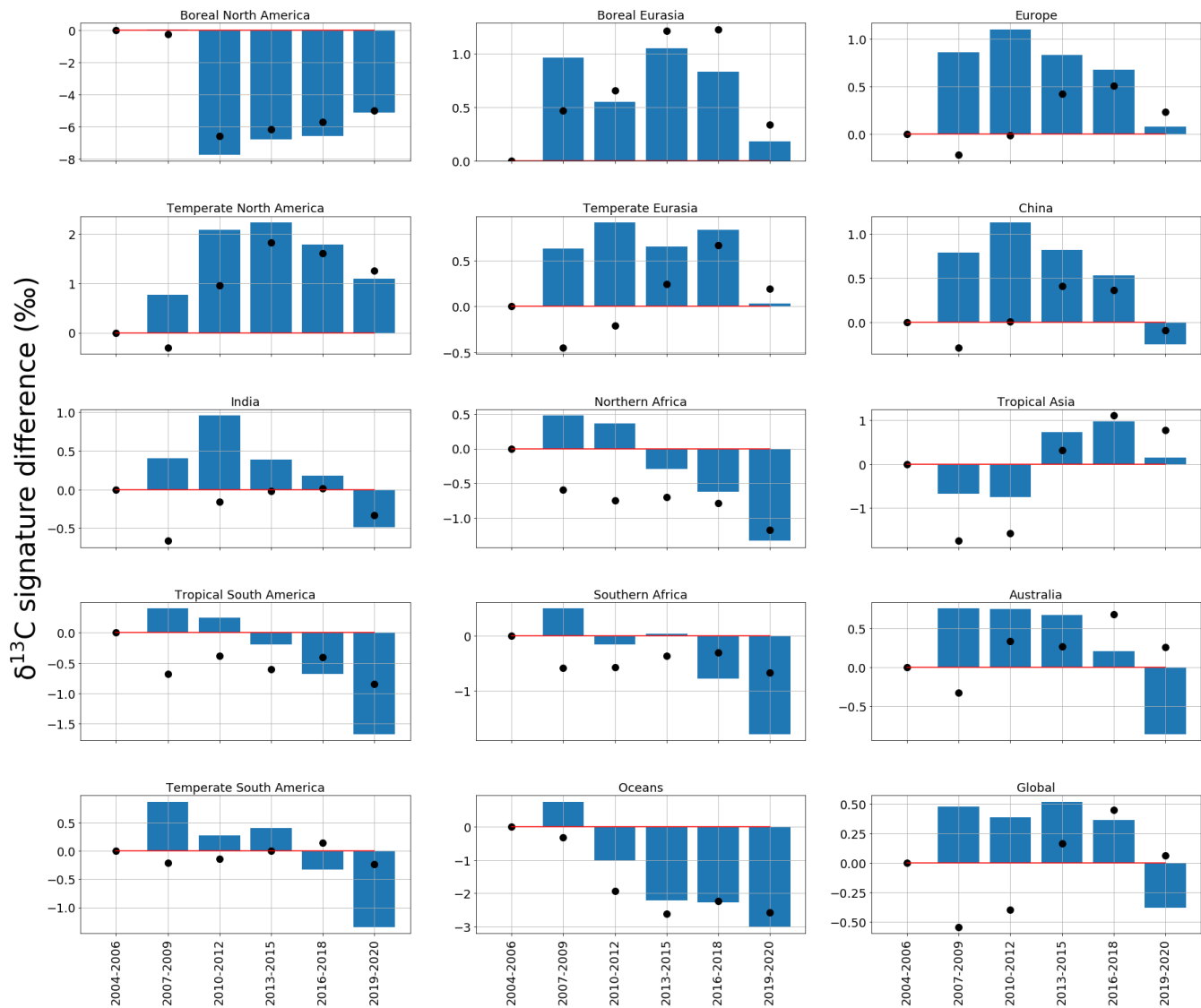


**Figure 5.** Regional and global *a posteriori*  $\delta^{13}\text{C}$  emissions source signatures (‰), in three-year groups (2004-06, 2007-09, 2010-12, 2013-15, 2016-18, 2019-20) as a residual from the 2004-06 *a posteriori* regional emissions source signature value. The *a priori* equivalent is represented by black dots. The regions are those solved for in the  $\text{CH}_4$  and  $\delta^{13}\text{C}$  inversions and are indicated by Figure 1.

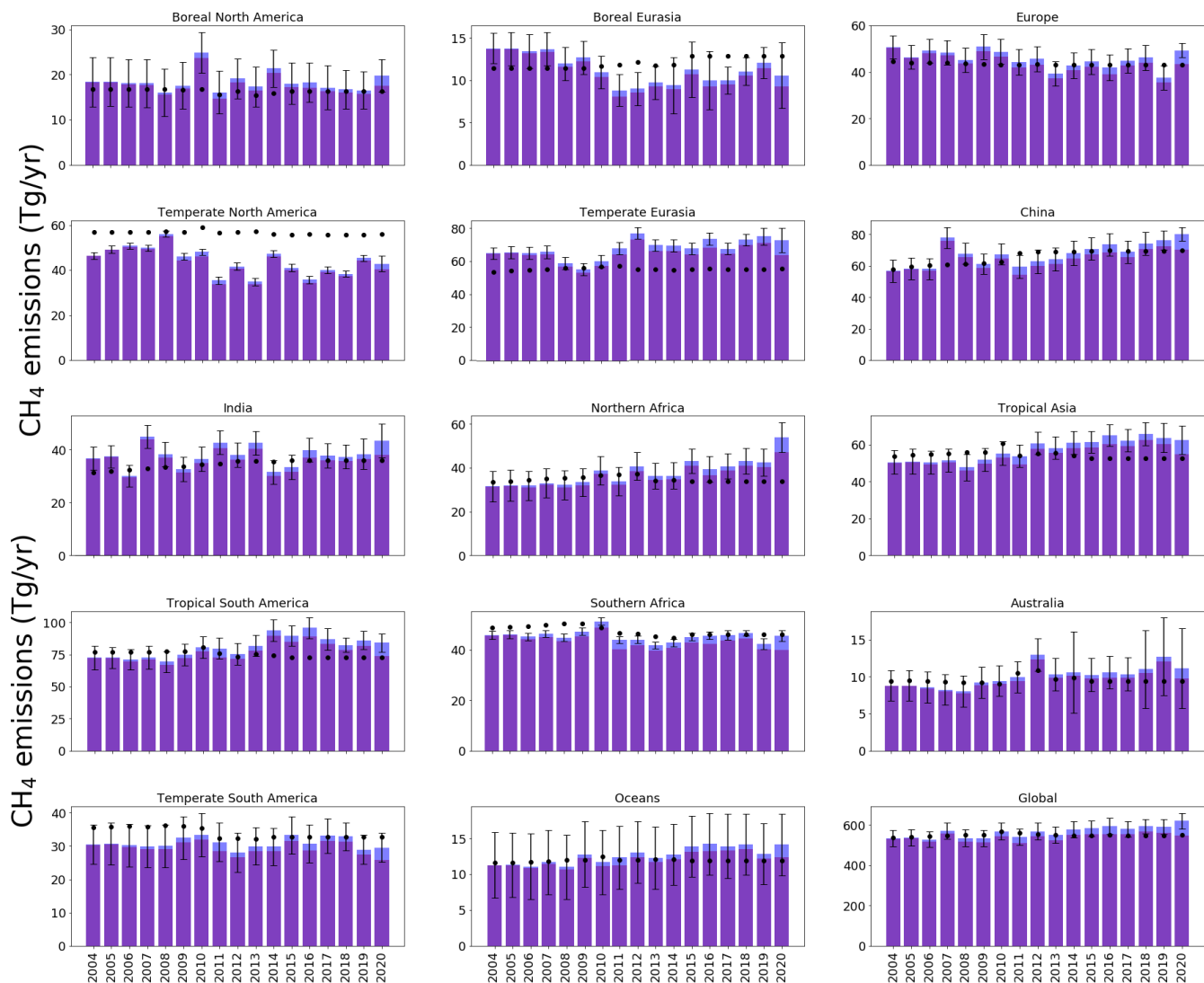


**Figure 6.** Annual mean CH<sub>4</sub> emissions (Tg/yr) for each region of the inversion (indicated by Figure 1) inferred from the ground-based data (dark blue) and the emissions estimates determined by a reduced OH values (described in the text, shown in red). A priori regional emissions estimates are indicated by black dots. Regional uncertainties for the a posteriori emissions are indicated.

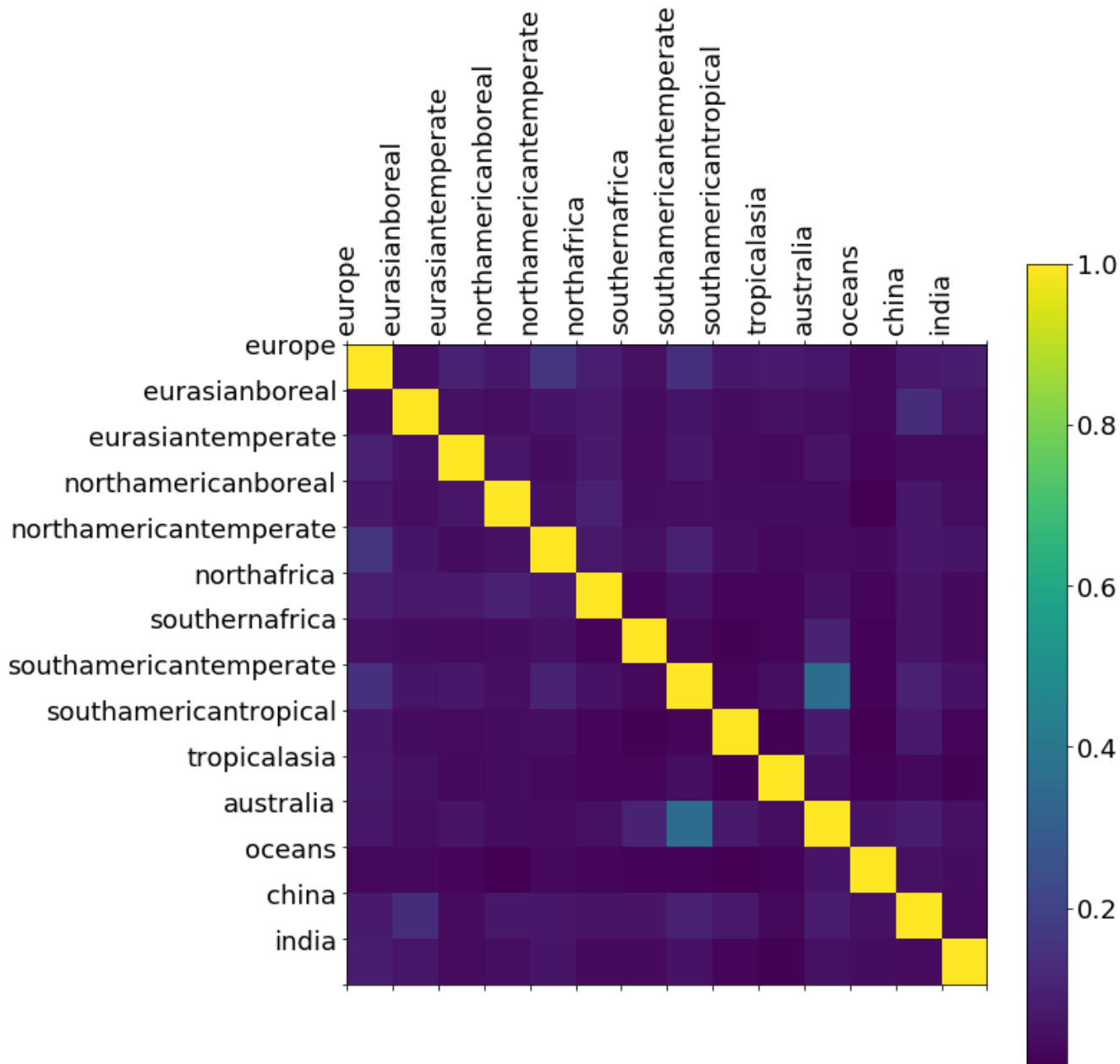


**Figure A1.** *A posteriori* correlations between CH<sub>4</sub> emissions from geographical regions inferred from ground-based CH<sub>4</sub> mole fraction data. These correlations are determined by normalising the diagonal elements of the *a posteriori* error covariance matrix (Eq. 2).



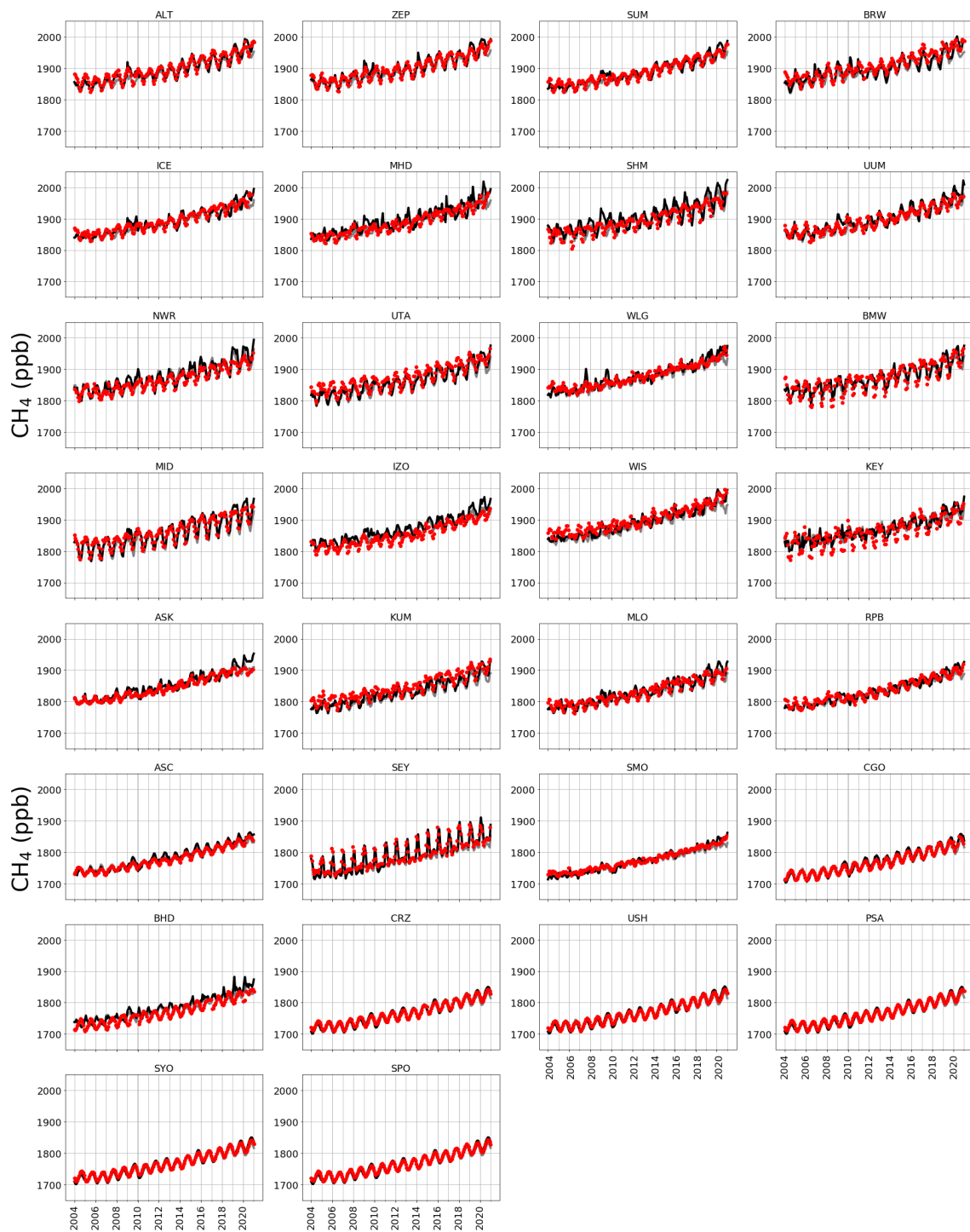


**Figure A2.** Observed (red dots), and *a priori* (grey), *a posteriori* (black) model atmospheric mole fractions at a series of NOAA sites (subplot titles denote site codes, Table A2), covering a range of latitudes.

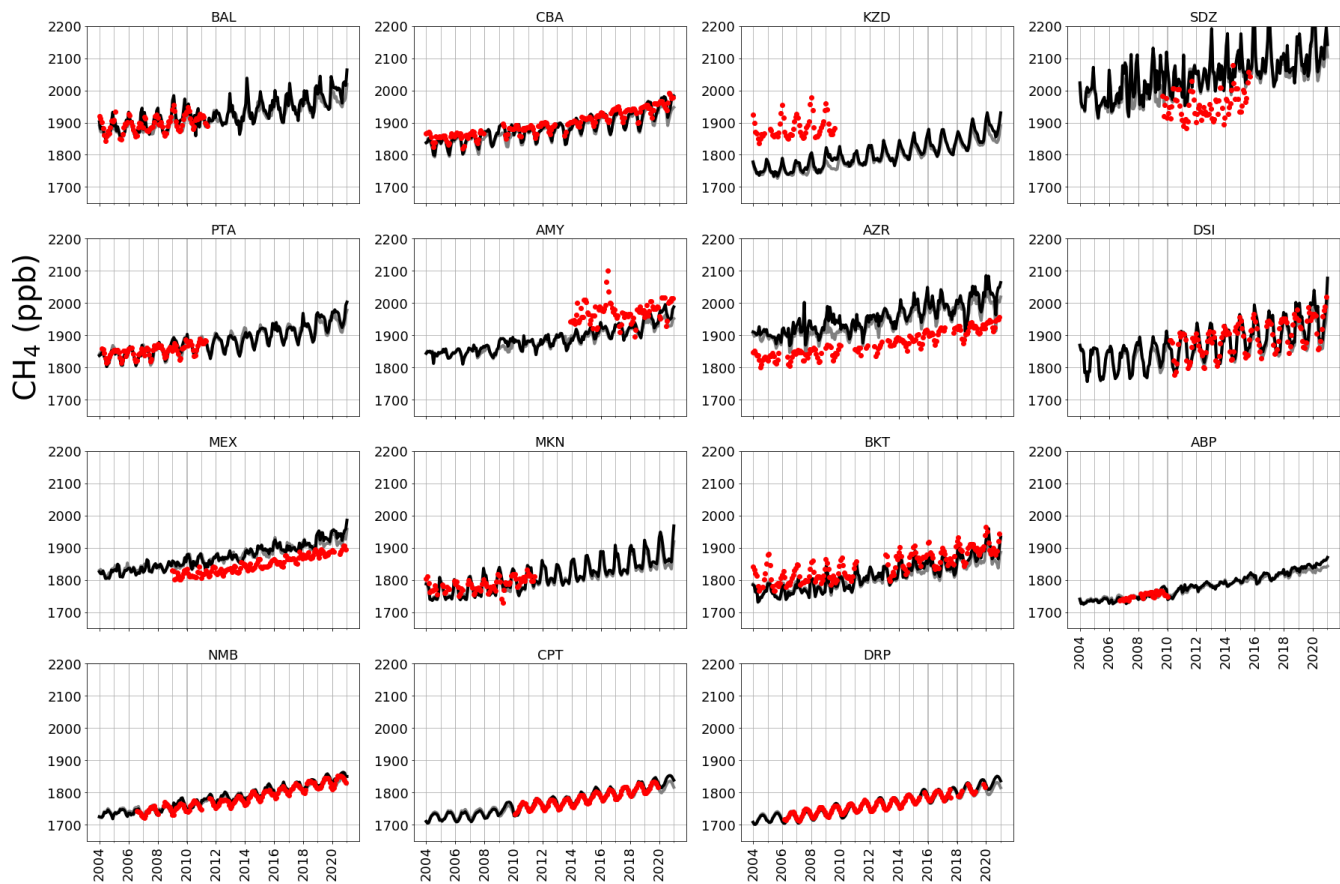


**Figure A3.** Left: Triennial  $A$  posteriori (black) monthly estimates of atmospheric  $\text{CH}_4$ , simulated at NOAA sites across latitudes. Red dots indicate monthly mean  $\text{CH}_4$  emission anomalies ( $\text{Tg/yr}$ ) data from 2004 to 2020 for ground-based the NOAA network sites indicated. These sites were not included in the  $\text{CH}_4$  inversion (denoted by shades of grey), but are shown here to provide independent validation of red  $A$  posteriori emissions. The sites included are: Baltic Sea, Poland ( $55.35^\circ\text{N}$ ,  $17.22^\circ\text{E}$ ) and from 2010 to 2020 for GOSAT inversion; Cold Bay, Alaska (denoted by shades of grey  $55.21^\circ\text{N}$ ,  $162.72^\circ\text{W}$ ); Sary Taukum, and triennial mean  $\delta^{13}\text{C}$  emissions source signatures Kazakhstan ( $44.08^\circ\text{N}$ , denoted by shades of blue  $76.87^\circ\text{E}$ ) from 2004 to 2020; Shangdianzi, all-grouped every 30 China ( $44.65^\circ$  latitude,  $117.12^\circ\text{E}$ ); Point Arena, USA ( $38.95^\circ\text{N}$ ,  $123.74^\circ\text{W}$ ); Anmyeon-do, Republic of Korea (i.e. blue  $36.54^\circ\text{N}$ , upper axis for  $\delta^{13}\text{C}$  results  $126.38^\circ\text{E}$ ); Terceira Island, red Azores ( $38.77^\circ\text{N}$ , lower axis for  $\text{CH}_4$  emissions results  $27.37^\circ\text{W}$ ); Dongsha Island, Taiwan ( $20.70^\circ\text{N}$ ,  $116.73^\circ\text{E}$ ); High Altitude Global Climate Observation Center, Mexico ( $18.98^\circ\text{N}$ ,  $97.31^\circ\text{W}$ ); Mt Kenya, Kenya ( $0.06^\circ\text{S}$ ,  $37.29^\circ\text{E}$ ); Bukit Kototabang, Indonesia ( $0.20^\circ\text{S}$ ,  $100.31^\circ\text{E}$ ); Arembepo, Brazil ( $12.77^\circ\text{S}$ ,  $38.17^\circ\text{W}$ ); Gobabeb, Namibia ( $23.58^\circ\text{S}$ ,  $15.03^\circ\text{E}$ ); Cape Point, South Africa ( $34.35^\circ\text{S}$ ,  $18.49^\circ\text{E}$ ); and Drake Passage ( $59.00^\circ\text{S}$ ,  $64.69^\circ\text{W}$ ).

A posteriori annual-mean atmospheric  $\text{CH}_4$  growth rate inferred from in-situ (black line) and GOSAT data (blue line) compared with the equivalent data as published by NOAA (red line, with uncertainty as blue surrounding field, Dlugokeneky et al., 2020). The green line denotes the annual atmospheric growth rate determined using the in situ mole fraction data from the sites included in the inversion ('Sites-Post'). To calculate the atmospheric growth rates from model calculations (Ground-Post and GOSAT-post), we compare the average global  $\text{CH}_4$  mole fraction in one year (the mean mole fraction of every grid box in every month of a year), with the mean value from the following year. The calculation is January-January, in order to remove the effects of the seasonal cycle, following the approach by NOAA (Dlugokeneky et al., 2020).

Annual-mean  $\text{CH}_4$  emissions ( $\text{Tg/yr}$ ) for each region of the inversion (indicated by Figure 1) inferred from the ground-based data (dark blue) and the emissions estimates determined by a reduced-OH values (described in the text, shown in red). A priori regional emissions estimates are indicated by black dots. Regional uncertainties for the a posteriori emissions are indicated.

Observed (red dots), and a priori (grey), a posteriori (black) model atmospheric mole fractions at a series of NOAA sites (subplot titles denote site codes, Table A2), covering a range of latitudes.

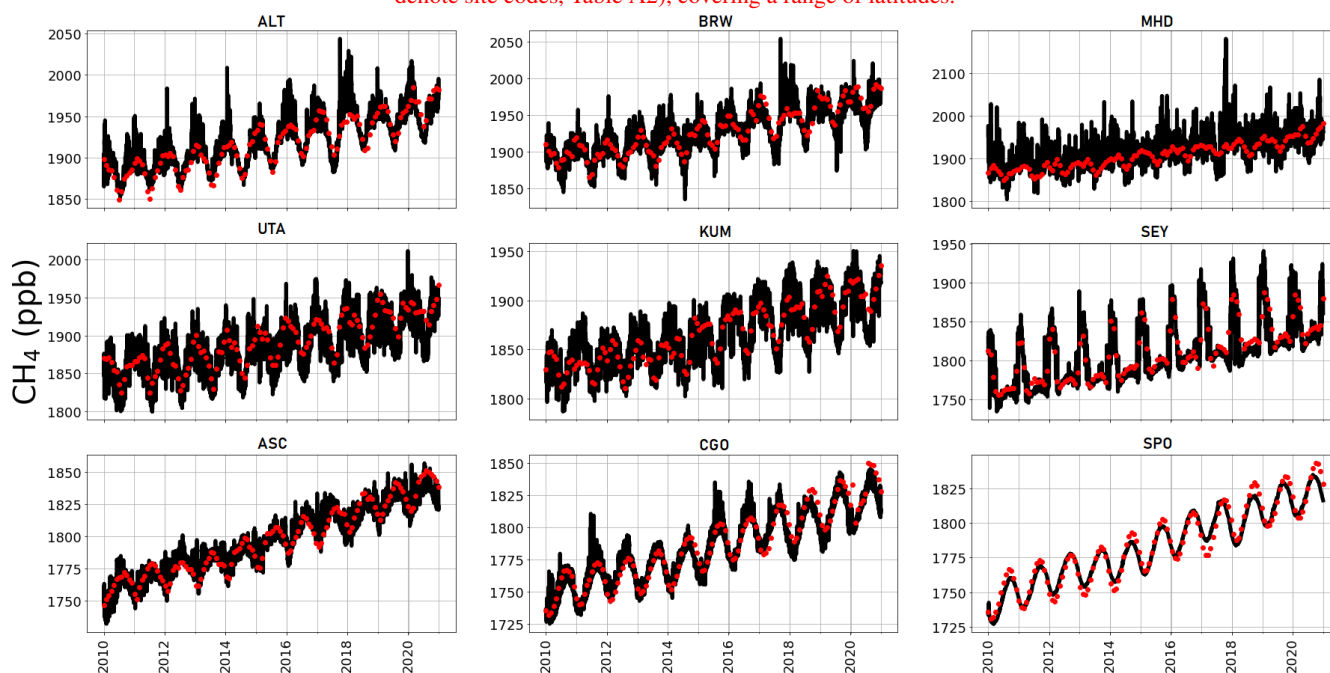


**Figure A4.** Observed (red dots), and three-hourly surface *a posteriori*  $\text{CH}_4$  values inferred from GOSAT data (black) at the location of a number of NOAA sites (Table A2) 2010-2020.

A posteriori correlations between  $\text{CH}_4$  emissions from geographical regions inferred from ground-based  $\text{CH}_4$  mole fraction data. These correlations are determined by normalising the diagonal elements of the a posteriori error covariance matrix (Eq. 2):

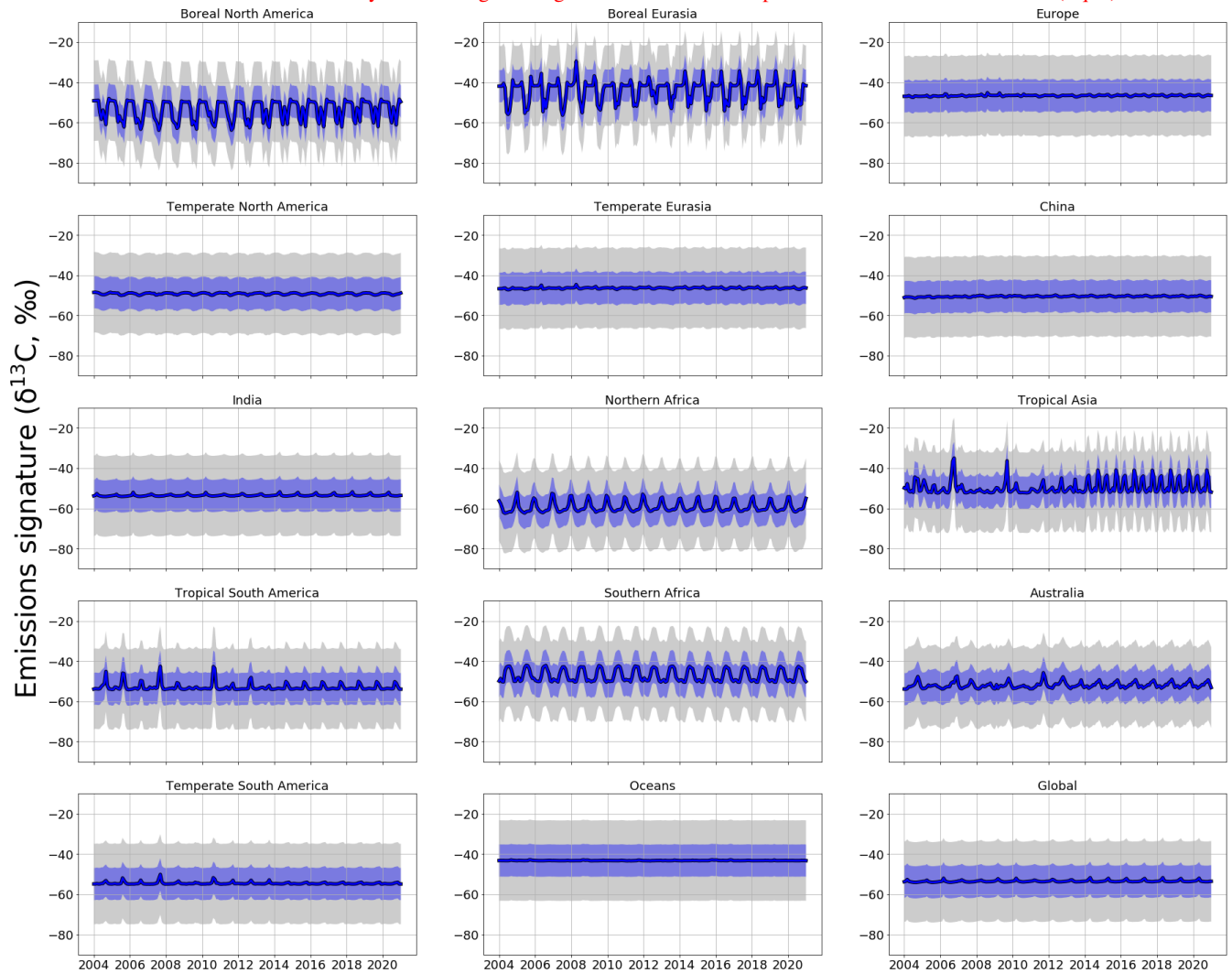


**Figure A5.** Monthly *a priori* (grey) and *a posteriori* (blue) regional  $\delta^{13}\text{C}$  source signatures (‰). Values are produced using ground-based *in situ*  $\delta^{13}\text{C}$  data. Uncertainties in source signatures are indicated as shaded envelopes, with *a priori* uncertainties of 15 %.

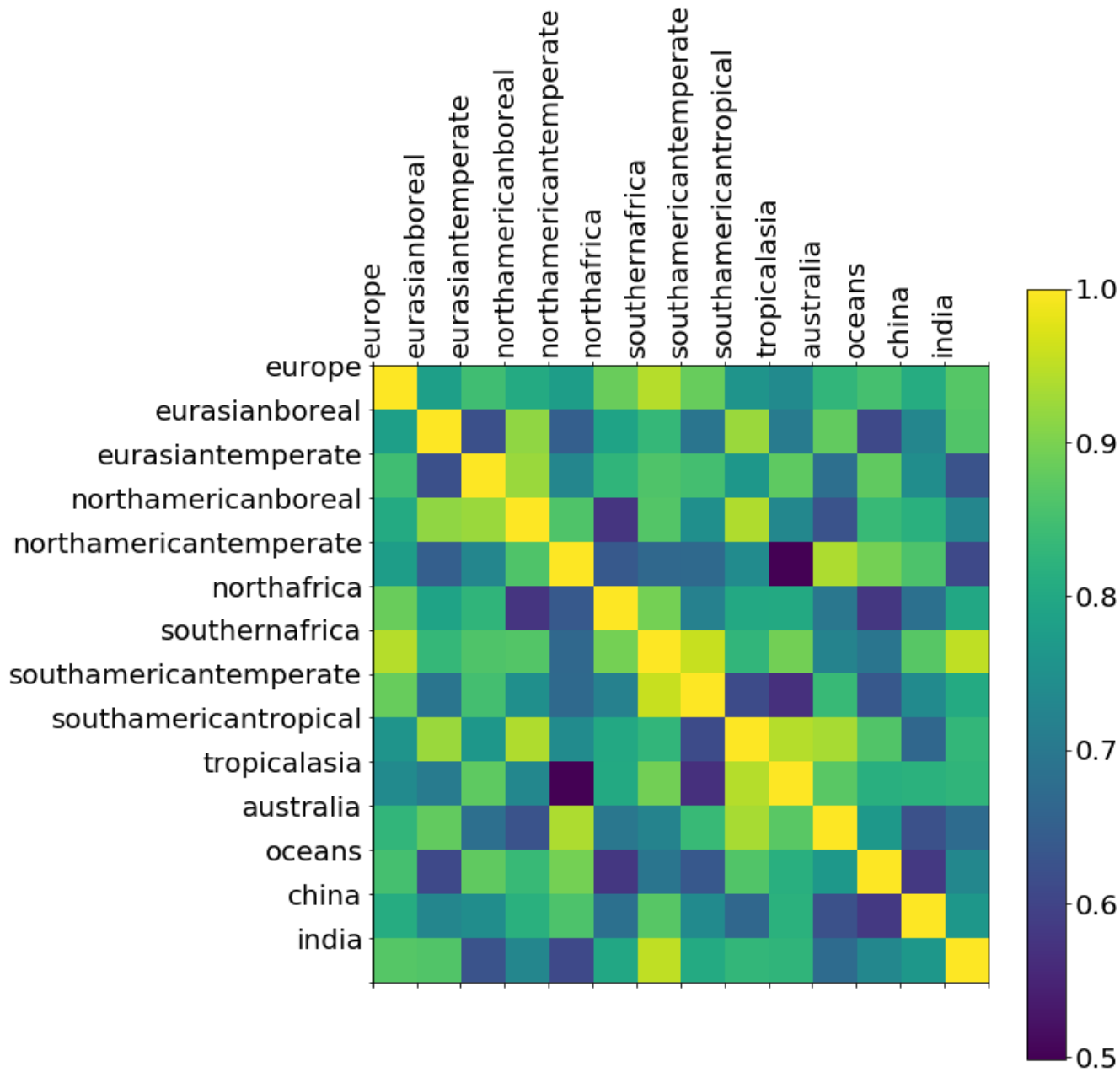


**Figure A6.** *A posteriori* correlations between  $\delta^{13}\text{C}$  source signatures from geographical regions inferred from ground-based  $\delta^{13}\text{C}$  data. These correlations are determined by normalising the diagonal elements of the *a posteriori* error covariance matrix (Equation Eq. 2).

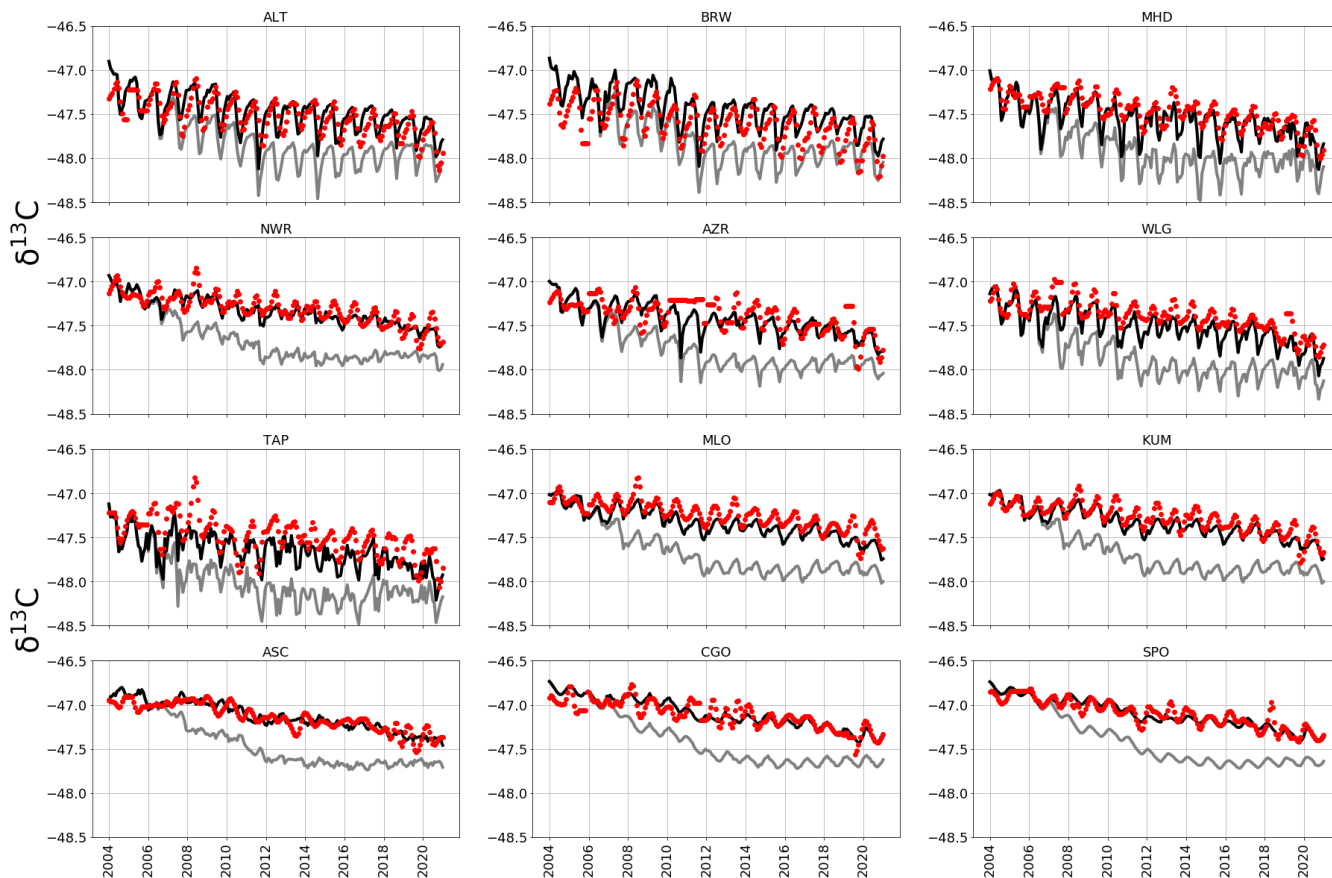


**Figure A7.** *A priori* (grey) and *a posteriori* (black) monthly estimates of atmospheric  $\delta^{13}\text{C}$ , simulated at NOAA sites across latitudes (site codes listed in Table A2). Red dots indicate monthly mean  $\delta^{13}\text{C}$  data from CU-INSTAAR for the respective sites.

790 ~~*A posteriori*(black) monthly estimates of atmospheric  $\text{CH}_4$ , simulated at NOAA sites across latitudes. Red dots indicate monthly mean  $\text{CH}_4$  data from the NOAA network sites indicated. These sites were not included in the  $\text{CH}_4$  inversion, but are shown here to provide independent validation of a posteriori emissions. The sites included are: Baltic Sea, Poland (55.35N, 17.22E); Sary-Taukum, Kazakhstan (44.08N, 76.87E); Shangdianzi, China (44.65N, 117.12E); Point Arena, USA (38.95N, 123.74W); Dongsha Island, Taiwan (20.70N, 116.73E); Mt Kenya, Kenya (0.06S, 37.29E); Arembepé, Brazil (12.77S, 38.17W); Cape Point, South Africa (34.35S, 18.49E); Drake Passage (59.00S, 64.69W).~~

**Table 1.** Global mean emissions of different CH<sub>4</sub> source types from bottom-up inventories (Saunois et al., 2020) and [our a posteriori emission estimates](#), and the corresponding conventional isotope ratios signatures (Sherwood et al., 2017). Uncertainties are shown as max-min values in square brackets.

<b>Source Type</b>	<b>Annual Mean Emission (Saunois)</b> <b>2003-2012 (Tg/CH<sub>4</sub>)</b>	<b>Annual Mean Emission (This Study)</b> <b>2004-2020 (Tg/CH<sub>4</sub>)</b>	<b>Isotopic Ratio</b> $\delta^{13}\text{C}_r$ (‰)
Gas and Oil	80 [68-92]	<u>82.0</u>	-44.0 [± 10.7]
Coal	42 [29-61]	<u>53.7</u>	-49.5 [± 11.2]
Livestock	111 [106-116]	<u>115.2</u>	-65.4 [± 6.7]
Waste	65 [60-69]	<u>67.9</u>	-56.0 [± 7.6]
Biomass Burning	17 [14-26]	<u>14.3</u>	-26.2 [± 4.8]
Termites	9 [3-15]	<u>11.9</u>	-63.4 [± 6.4]
Wetlands	149 [102-182]	<u>170.9</u>	-61.5 [± 5.4] (Tropical) -71.5 [± 5.4] (Arctic)
Rice	30 [25-38]	<u>30.7</u>	-62.2 [± 3.9]

**Table A1.** Kinetic Isotope Effects (KIEs) for different isotopologues reacting with the three main sinks of CH<sub>4</sub> (OH, Cl, soil) at 298 K. A KIE indicates relative reaction rate compared with <sup>12</sup>CH<sub>4</sub>; the reaction rate constant is applied to the OH and Cl sinks and is dependent upon temperature (T); and the scaling factor is applied to the soil sink at each timestep (handled as a negative emission).

Isotopologue	Sink	KIE	Reaction Rate Constant	Scaling Factor	Literature Source
<sup>12</sup> CH <sub>4</sub>	OH	1	$2.45 \times 10^{-12} \times e^{\frac{-1775}{T}}$	n/a	Burkholder et al., 2019
<sup>12</sup> CH <sub>4</sub>	Cl	1	$9.600 \times 10^{-12} \times e^{\frac{-1360}{T}}$	n/a	Kirschke et al., 2013
<sup>12</sup> CH <sub>4</sub>	soil	n/a	n/a	1	Snover and Quay, 2000
<sup>13</sup> CH <sub>4</sub>	OH	1.0039	$2.44 \times 10^{-12} \times e^{\frac{-1775}{T}}$	n/a	Burkholder et al., 2019
<sup>13</sup> CH <sub>4</sub>	Cl	1.06	$9.057 \times 10^{-12} \times e^{\frac{-1360}{T}}$	n/a	Feilberg et al., 2005
<sup>13</sup> CH <sub>4</sub>	soil	n/a	n/a	1.0670	Snover and Quay, 2000



**Table A2.** Sites that are included in the *in situ* inversions. All sites are part of the NOAA network, other than KRS, which is part of the JR-STATION network, monitored by NIES Japan.

<b>Code</b>	<b>Full Name</b>	<b>Latitude</b>	<b>Longitude</b>
ALT	Alert Station	82.28	-62.30
ZEP	Ny-Alesund, Svalbard	78.90	11.89
SUM	Summit, Greenland	72.60	-38.42
BRW	Barrow Station	71.32	156.61
ICE	Storhofdi,Iceland	63.40	-20.29
KRS	Karasevoe, Siberia	58.14	82.25
MHD	Mace Head, Ireland	53.33	-9.90
SHM	Shemya Island, Alaska	52.71	174.12
UUM	Ulaan Uul, Mongolia	44.45	111.09
NWR	Niwot Ridge, Colorado	40.05	-105.59
UTA	Wendover, Utah	39.90	-113.72
WLG	Mt. Waliguan, China	36.29	100.90
BMW	Bermuda	32.26	-64.88
WIS	Ketura, Israel	29.96	35.06
IZO	Izana, Tenerife	28.31	-16.50
MID	Midway Islands	28.22	-177.37
KEY	Key Biscane, Florida	25.67	-80.16
ASK	Assekrem, Algeria	23.26	5.63
KUM	Cape Kumukahi, Hawaii	19.56	-154.89
MLO	Mauna Loa, Hawaii	19.54	-155.58
RPB	Ragged Point, Barbados	13.17	-59.43
SEY	Mahe Island, Seychelles	-4.68	55.53
ASC	Ascension Island	-7.97	-14.40
SMO	American Samoa	-14.25	-170.56
CGO	Cape Grim	-40.68	144.69
BHD	Baring Head	-41.40	174.87
CRZ	Crozet Island	-46.43	51.85
USH	Ushuaia, Argentina	-54.84	-68.31
PSA	Palmer Station, Antarctica	-64.77	-64.05
SYO	Syowa Station, Antarctica	-69.01	39.59
SPO	South Pole, Antarctica	-89.98	-24.8